PHYSICS OF THE HELICON ANTENNA ON THE PROTOTYPE MATERIALS EXPOSURE EXPERIMENT

BY

PAWEL A. PIOTROWICZ

THESIS

Submitted in partial fulfillment of the requirements
for the degree of Master of Science in Nuclear, Plasma, and Radiological Engineering
in the Graduate College of the
University of Illinois at Urbana-Champaign, 2018

Urbana, Illinois

Master's Committee:

Professor David N. Ruzic, Chair
Assistant Professor Davide Curreli

Abstract

Proto-MPEX has been operating in a high-density helicon-mode of operation. The helicon mode of operation is classified by an increase in target on-axis electron density ($< 6e19\ m^{-3}$) and a decrease in electron temperature ($23\ eV$) during a helicon pulse. This transition is observed when Deuterium gas is puffed into the device and is dependent on operating configurations. The Proto-MPEX helicon antenna is a quarter turn right handed helical twist antenna powered by RF at 13.56 MHz and > 110 kW of power. Establishing plasma densities and magnetic field strengths under the antenna that suppress non-resonant mode conversion to the slow-wave are thought to be responsible for operating in the "helicon-mode". Evidence for this phenomena to be responsible for the "helicon-mode" of operation is presented.

The experimental results showing evidence of this phenomena are presented here. First, we present time-resolved measurements of an edge-to-core power transition during a "helicon-mode" plasma pulse in the form of infra-red camera imaging of a thin stainless steel target plate. The time-resolved images measure the two-dimensional distribution of power deposition in the helicon discharge. The discharge displays a mode transition characterized by a significant increase in the on-axis electron density and core power coupling, suppression of edge power coupling and the formation of a fast-wave radial normal mode. Although the self-consistent mechanism that drives this transition is not yet understood, the edge-to-core power transition displays characteristics that are consistent with the discharge entering a slow-wave anti-resonant regime. RF magnetic field measurements made across the plasma column, together with the power deposition results, provide direct evidence to support the suppression of the slow-wave in favour of core plasma production by the fast-wave in a light-ion helicon source.

A full wave model of the helicon antenna has been made in the finite element analysis software, COMSOL Multiphysics, to investigate the wave fields produced and the power deposition inside the Proto-MPEX device. Core electron density and magnetic field under the helicon is scanned while tracking core power deposition. The peaks of core power deposition in this parameter space are then investigated and the propagating modes are analyzed. These areas of increased core power deposition are then identified as helicon normal modes that are predicted to decrease edge coupling of power and increase core power coupling

by suppressing the non-resonant mode conversion of the fast-wave to the slow-wave in the periphery of the plasma.

Table of Contents

List of Tables

List of Figures

List of Abbreviations

AR	Anti-Resonance
HM	Helicon Mode
FW	Fast-Wave
SW	Slow-Wave
TG	Trivelpiece Gould Mode
ES	Electro-Static
EM	Electro-Magnetic
HDLH	High-Density limit to the Lower-Hybrid resonance
MPEX	Materials Plasma Exposure eXperiment
Proto-MPEX	Prototype Materials Plasma Exposure eXperiment
PMI	Plasma Materials Interactions
PFC	Plasma Facing Components

List of Symbols

n_e	Electron density/Plasma density
n_i	Ion density
n_0	Neutral gas density
P_0	Neutral gas pressure
B_0	DC magnetic field strength
m_e	Electron mass
m_i	Ion mass
k_0	Vacuum wave-number
$\hat{r}$	Radial coordinate
$\hat{\phi}$	Azimuthal coordinate
$\hat{z}$	Axial coordinate
$\bar{B}_r$	$\hat{r}$ Component of the DC magnetic field
$\bar{B}_\phi$	$\hat{\phi}$ Component of the DC magnetic field
$\bar{B}_z$	$\hat{z}$ Component of the DC magnetic field
B_r	$\hat{r}$ Component of the RF magnetic field
B_ϕ	$\hat{\phi}$ Component of the RF magnetic field
B_z	$\hat{z}$ Component of the RF magnetic field
E_r	$\hat{r}$ Component of the RF electric field
E_ϕ	$\hat{\phi}$ Component of the RF electric field
E_z	$\hat{z}$ Component of the RF electric field
ω_{ce}	Electron cyclotron frequency
ω_{ci}	Ion cyclotron frequency
ω_{pe}	Electron plasma frequency
ω_{pi}	Ion plasma frequency
ω	Driving frequency

$\vec{k}$	Wave vector
k_z	Axial wave-number
$k_\perp$	Perpendicular wave-number
n	Index of refraction
n_z	Axial index of refraction

Chapter 1

Introduction

This chapter will first introduce the motivation for developing plasma material interaction (PMI) facilities. Section 1.1 will present the current issues and knowledge gaps with material compatibility in fusion reactors. This will also go over the motivation for developing a new PMI facility planned to be constructed at Oak Ridge National Laboratory (ORNL) called the Plasma Materials Exposure eXperiment (MPEX). This chapter will go over the requirements required for such a facility and the approach to attain these parameters. Currently, the Prototypical Plasma Materials Exposure eXperiment (Proto-MPEX) device is operational at ORNL and is being used to develop the source concepts for MPEX. A helicon plasma source is installed currently on Proto-MPEX device and is operated with $>$ 100 kW, producing an electron density of $n_e > 6e19\ m^{-3}$. Section 1.2 will present the motivation for using a helicon antenna as a plasma source for Proto-MPEX. Here we will also describe some differences in operating a helicon source with a molecular light ion gas (Deuterium) and a inert heavy ion gas (Argon).

1.1 Material Compatibility for Fusion Reactors

Understanding the science of plasma material interactions (PMI) will be critical to developing plasma facing components (PFC) for the exploitation of fusion energy. Three major challenges need to be addressed on the road to commercial fusion reactors, 1) Power exhaust, 2) PFC lifetime, and 3) Tritium retention. Present technology is able to handle 10 MWm^{-2} heat fluxes. ITER is designed to maintain the heat flux of < 10 MWm^{-2}. This corresponds to parallel plasma heat flux of about 80 MWm^{-2}, that will strike the divertor, in addition to the heating from radiation and neutral particles. In addition to these high heat fluxes PFCs are exposed to large ion fluxes ($\Gamma > 10^{24} m^{-2} s^{-1}$) which will lead to material erosion and re-deposition of material as well as surface modification of the surface. The conditions of the plasma interaction with the materials surface can vary from a dense and cold plasma (T_e 1 eV, $n_e > 2 \times 10^{21}\ m^{-3}$) to a hot lower density plasma ($5 < T_e < 20\ eV$, $10^{19} < n_e < 10^{21}\ m^{-3}$). These plasma conditions will dictate regions of errosion and deposition on the PFC surface and need to be studied. Tritium retention of a material is another issue

that needs to be addressed, currently experiments are limited to fluence levels of $10^{27} - 10^{28}$ D/m^2. To address the issue of tritium retention experiments are needed that are capable of attaining fluences beyond the 10^{28} D/m^2 [1, 2, 3]

1.1.1 The Materials Plasma Exposure eXperiment

Many expert panel reports have concluded that the knowledge gaps associated with PMI need to be urgently addressed [4, 5]. The 2012 FESAC report [6] stated that the current facilities in the US are no longer unique or world leading and cannot answer outstanding scientific questions associated with PMI. The report continues to state that, moderate investments in medium scale facilities can lead to high-impact fusion research. Oak Ridge National Laboratory (ORNL) is developing the source technology for the new Material-Plasma Exposure eXperiment (MPEX) facility that would address the outstanding questions associated with PMI. Some of the specifications for the MPEX facility will fulfill are power fluxes of 20 MWm^{-2}, inclined target ($B_0 > 1$ T), steady state up to $10^6 sec$, including exposure of liquid metal targets, neutron-irradiated samples with significant dpa, and independent control of T_e and T_i. Some linear devices address part of these requirements but not all of them. Table 1.1 summarizes the capabilities of MPEX versus the PISCES and MAGNUM facilities.

Table 1.1: Comparison table of the current linear PMI experiments vs MPEX proposed parameters.

Parameter / Capability	MPEX	PISCES	Magnum
Steady-state heat flux (90°) $[MWm^{-2}]$	≥ 10	≈ 10	≥ 10
Steady-state heat flux (5°) $[MWm^{-2}]$	3	N/A	N/A
Target T_e $[eV]$	1-15	N/A	≤ 5
Ion flux $[m^{-2}s^{-1}]$	$10^{21} - 10^{19}$	$\leq 10^{19}$	$10^{22} - 10^{19}$
Annual Fluence	10^{31}	10^{29}	10^{31}
Surface morphology changes	Y	N	Y
Neutron irradiated samples	Y	N	N
Divertor component mockups	Y	N	Y

The MPEX device is planned to be a steady-state device utilizing superconducting magnet coils and RF technology to source and heat the plasma. The plasma source currently planned for MPEX is a helicon source chosen for it's high ionization efficiency. The plasma is then heated with auxiliary heating to heat the electrons and ions independently. The electron heating is planned to be carried out by 28 GHz Electron-Bernstein Wave (EBW) heating. While the ion heating will be achieved by the "beach-heating" method [2, 1, 3]. This thesis will focus on the helicon source installed on Proto-MPEX.

1.2 Helicon Sources

Ever since Boswell published on the ionization efficiency of inductively coupling RF waves to the natural oscillations in a plasma column[7, 8], helicon plasma sources have gained interest in many applications. Some areas of research that have found application for helicon sources are semiconductor processing [9, 10] and space propulsion [11, 12]. A recent application of helicon sources has been as plasma sources for fusion-relevant plasma-material interactions (PMI) investigation [3, 1, 13, 14, 15, 2, 16]. However, in order for helicon sources to be relevant to PMI investigation, they must be able to produce high-density plasmas with light ion fuels (H_2, D_2, He). In this work I will show that the conditions in Proto-MPEX necessitate significant contribution from the fast wave in power deposition to attain high electron density with the helicon source.

Most authors attribute the efficient ionization of helicon sources in heavy ion discharges to the collisional damping of the Trivelpiece Goulde mode (TG) [17, 18, 19, 20, 21]. The TG mode, slow-wave, is typically excited through non-resonant mode conversion of the helicon mode, fast-wave, that occurs at the periphery of the plasma[22], therefore power deposition is typically edge dominated in helicon sources using heavy ions. Chen and Curreli[21, 20] have shown that regardless of where the ionization occurs, the centrally peaked profile in heavy ion helicon discharges can be explained by the short circuit effect. The short circuit effect is restricted to short discharges with unmagnetized ions. In discharges using light ions, this effect is then typically not applicable and hollow density profiles are observed when significant core power deposition is not observed[23].

In this thesis results are presented from the helicon source in the Prototype Material Exposure eXperiment (Proto-MPEX) [2]. An improved mode of operation has been recently observed [2, 23] and is characterized by a significant increase in the on-axis electron density ($n_e \approx 1 - 6 \times 10^{19}\ m^{-3}$), a change in the radial density profile from hollow to centrally peaked, and a change in the radial electron temperature profile from hollow to flat. Evidence is presented here to show that the improved mode of operation is due to strong power coupling to the core plasma via the fast-wave and suppression of mode conversion to the slow-wave at the edge. Radial eigenmode formation of the fast-wave is concurrently observed with the transition from edge to core power coupling in the plasma column. Chapter 3 will go over these experimental observations during "helicon-mode" operation on Proto-MPEX. Next, I will describe a 2D axisymmetric model used to identify the fast-wave normal modes in Proto-MPEX that are responsible for the "helicon-mode" in chapter 4. Chapter 5 describes the results from the computational model which agree qualitatively with experimental observations of slow-wave suppression during the "helicon-mode" operation in Proto-MPEX. Conclusions and extension to this work are presented in Chapter 6.

1.2.1 Light Ion Helicon Sources

There are two main aspects that make light-ion helicon sources different from heavy-ion sources: ion magnetization and the effect of the lower hybrid resonance. At high densities, the lower hybrid resonance has the effect of restricting the slow-wave to a very thin layer in the plasma periphery and creates an evanescent layer between the fast-wave in the high plasma density region (core) and the slow-wave in the low plasma density region (edge) of the discharge [24]. Ion magnetization precludes transport effects that cause centrally peaked electron density profiles in heavy-ion discharges [20, 21]. Therefore in discharges with strongly magnetized ions and electrons, production of centrally peaked density profiles necessitates the deposition of power directly at the core. This mechanism is only accessible via the fast-wave.

Light ion helicon sources have proven more difficult to achieve high-density plasmas with[24, 25] than heavy ion helicon sources. Sakawa[24] showed that for a helicon source fueled with D_2 and H_2 gas, electron density would reach a maximum at $B_0 \approx 0.02$ T then sharply fall off. This is not the case using Ar gas to fuel the discharge, which would show a linear increase in electron density past $B_0 = 0.15$ T. That work then showed that the reduced ion mass moves the high-density limit of the lower hybrid resonance (HDLH), which reduces to the root of the product of the electron and ion cyclotron frequencies as $\omega_{HDLH} = \sqrt{\omega_{ce}\omega_{ci}}$, to lower magnetic field values. Operating in magnetic field values above the HDLH, $B_0 0.02$ T for D_2, restricts the slow-wave to the low electron density region of the plasma column and the helicon wave to the high-density region, thus creating a region in the plasma that is evanescent to both waves. Light and Chen[25] later showed that low-frequency instabilities that have characteristics of the resistive drift wave instability and the Kelvin-Helmholtz instability were more prevalent in plasmas with light ion mass operating above the HDLH. Another difficulty associated in working with Deuterium gas is that it naturally exists as a molecular gas. Molecular gas presence in a plasma opens more avenues of power loss in the form of rotational and vibrational excitation cross sections.

Several devices have been able to achieve high electron densities in light ion plasmas[26, 27, 14, 2, 23] operating in magnetic fields above the HDLH. These devices all used a converging magnetic field geometry. However, the effect of this magnetic geometry on the success of these devices is not understood. Mori[26] measured fast-wave radial normal modes on the mini-RFTF devices and attributed their excitation to the variation of electron density with the magnetic field. On the Proto-MPEX device, the "helicon-mode" is attributed to exciting radial normal modes of the fast-wave in the plasma column[2, 23].

Chapter 2

Theory

This chapter will give an overview of the relevant theory related to describing wave propagation in helicon antennas. Section 2.1 will present a derivation of the cold plasma tensor and how to arrive at a dispersion relation. Section 2.2 will explain how the plasma wave couples power to a strongly collisional plasma. How geometry affects and boundary conditions affect wave propagation will be described in section 3.3. In this section the cylindrically bound dispersion relationship will be derived. Finally, a discussion and a simple picture of mode conversion in a helicon sources will be presented in section 2.5.

2.1 Cold Plasma Wave Theory

One way to understand wave propagation in a plasma is to derive dielectric properties of the plasma based on it's characteristic properties such as the electron density (n_e), the background magnetic field strength (B_0), electron (m_e) and ion (m_i) mass. From these properties it is possible to solve for a plasma current based on the particle velocity, its charge, and density. To solve for the particle velocity one can take many approaches, the most straightforward to formulate is to take the equation of motion of a single particle and assume zero temperature for both the electrons and ions. This approach is able to adequately describe wave propagation in a "cold plasma", in which finite temperature effects can be neglected. The following section outlines the derivation of the STIX tensor which contains the dielectric properties of a cold plasma [28]. Then a general dispersion relation will be obtained from the STIX tensor which can reduced to a quadratic formula for the square of the index of refraction (n^2). The quadratic form of the dispersion relation signifies that there exists two wave solutions for a set of plasma properties. These waves will have different characteristic length scales and propagation characteristics. The phase velocity of the wave will be presented and the meaning and uses of it will be discussed. The group velocity (v_g) of the wave can also be derived from the dispersion relation. The angle of the group velocity from the magnetic field dictates the direction the electromagnetic energy of the wave will propagate in the plasma.

2.1.1 STIX Tensor Derivation

To start the derivation of the STIX tensor we must write an equation that will allow us to solve for velocity of the electron and ion particles. The cold plasma approximation allows us to write the equation of motion for a single charged particle.

$$m_j \frac{dv_j}{dt} = q_j(\vec{E} + \vec{v} \times \vec{B}) \tag{2.1}$$

In Eq. 2.1 the properties of particle j are the mass (m_j), velocity (v_j), and charge q_j. The forces present on the charge are the electric charge from the electric field ($\vec{E}$), and the magnetic field ($\vec{B}$). Next we write Maxwell's equations.

$$\nabla \times \vec{E} = -\frac{\partial \vec{B}}{\partial t} \tag{2.2}$$

$$\nabla \times \vec{B} = \mu_0(\vec{J} + \frac{\partial \vec{D}}{\partial t}) \tag{2.3}$$

Where if we set $D = \epsilon_0 \vec{E}$ then Eq. 2.2 and 2.3 describe the propagation of electromagnetic waves in vacuum with a current source ($\vec{J}$) given by the charged particles present in the plasma. We then write the current as a function of the charged particle's density, charge, and velocity; then sum over the particle species present in the plasma.

$$\vec{J} = \sum_j (n_j q_j \vec{v}_j) \tag{2.4}$$

Next Fourier transform Eq. 2.1, 2.2, and 2.3 which amounts to approximating the spatial variation of the components as plane waves with the wavevector given by $\vec{k}$, and temporal variation of the wave components with a frequency given by ω.

$$\vec{E} = \vec{E_1} e^{i(\vec{k} \bullet \vec{r} - \omega t)} \tag{2.5}$$

$$\vec{B} = B_0 \hat{z} + \vec{B_1} e^{i(\vec{k} \bullet \vec{r} - \omega t)} \tag{2.6}$$

$$\vec{v} = \vec{v_1} e^{i(\vec{k} \bullet \vec{r} - \omega t)} \tag{2.7}$$

From Eq. 2.6 we see that we expanded the magnetic field into a DC component given by B_0 that is oriented in the $\hat{z}$ direction and an RF component with plane wave variation. In the equation of motion we have also ignored the RF magnetic field approximating that it is much weaker than the DC component. We have

simplified terms that contain the ion cyclotron frequency $\omega_{cj} = \frac{q_j B_0}{m_j}$. Next we use the definitions given by Eq. 2.5 through 2.7 in Eq. 2.1 and solve for the particle velocity.

$$v_{xj} = \frac{iq_j}{m_j(\omega^2 - \omega_{cj}^2)}(\omega E_x + i\omega_{cj} E_y) \tag{2.8}$$

$$v_{yj} = \frac{iq_j}{m_j(\omega^2 - \omega_{cj}^2)}(-i\omega_{cj} E_x + \omega E_y) \tag{2.9}$$

$$v_{zj} = \frac{iq_j}{m_j \omega} E_z \tag{2.10}$$

To simplify Eq. 2.8 and 2.9 we can introduce the rotating coordinate system such that $v_\pm = v_x \pm i v_y$ and $E_\pm = E_x \pm i E_y$.

$$v_\pm = \frac{iq_j}{m_j(\omega \mp \omega_{cj})} E_\pm \tag{2.11}$$

We can then write the plasma current in the rotating coordinate system as.

$$J_\pm = i\epsilon_0 \sum \frac{iq_j}{m_j(\omega \mp \omega_{cj})} E_\pm \tag{2.12}$$

$$J_z = i\epsilon_0 \sum \frac{\omega_{pj}^2}{\omega} E_z \tag{2.13}$$

Here we introduce the plasma frequency given by $\omega_{pj}^2 = \frac{n_j q_j}{\epsilon_0 m_j}$. Now we can define the displacement current caused by the presence of the plasma as follows.

$$\vec{J} - i\omega\epsilon_0 \vec{E} \equiv -i\omega\epsilon_0 (\overleftrightarrow{K} \bullet \vec{E}) \tag{2.14}$$

From Eq. 2.14 we can solve for the terms of the dielectric tensor $\overleftrightarrow{K}$, and organize the tensor with STIX notation given as follows.

$$\overleftrightarrow{K} = \begin{bmatrix} S & -iD & 0 \\ iD & S & 0 \\ 0 & 0 & P \end{bmatrix} \tag{2.15}$$

The terms given in Eq. 4.17 are defined as follows.

$$S = \frac{1}{2}(R + L) \tag{2.16}$$

$$D = \frac{1}{2}(R - L) \tag{2.17}$$

$$P = 1 - \sum_j \frac{\omega_{pj}^2}{\omega^2} \tag{2.18}$$

$$R = 1 - \sum_j \frac{\omega_{pj}^2}{\omega(\omega + \omega_{cj})} \tag{2.19}$$

$$L = 1 - \sum_j \frac{\omega_{pj}^2}{\omega(\omega - \omega_{cj})} \tag{2.20}$$

With the STIX tensor now defined we can use this tensor to describe the dielectric properties of the plasma of interest and solve Mawell's equations in the presence of a cold plasma.

2.1.2 Dispersion Relation

With the STIX tensor defined and the displacement current in place of the the plasma current. We can now rewrite Maxwell's equations as follows:

$$i\vec{k} \times \vec{E} = -i\omega\vec{B} \tag{2.21}$$

$$i\vec{k} \times \vec{B} = -i\omega\epsilon_0\mu_0\overleftrightarrow{K} \bullet \vec{E} \tag{2.22}$$

We can now reorganize Eq. 2.21 and 2.22 into the Helmholtz equation given by

$$\vec{n} \times (\vec{n} \times \vec{E}) + \overleftrightarrow{K} \bullet \vec{E} = 0 \tag{2.23}$$

$$\vec{n} = \frac{\vec{k}c}{\omega} \tag{2.24}$$

Assuming now that θ is the angle between $\vec{k}$ and B_0 we can expand Eq. 2.23 to the following matrix equation.

$$\begin{pmatrix} S - n^2 cos^2\theta & -iD & n^2 cos\theta sin\theta \\ iD & S - n^2 & 0 \\ n^2 cos\theta sin\theta & 0 & P - n^2 sin^2\theta \end{pmatrix} \begin{pmatrix} E_x \\ E_y \\ E_z \end{pmatrix} = 0 \tag{2.25}$$

Here we see that any non-trivial solution to the wave equation requires the determinant of the coefficient matrix to vanish. This condition can be summarized as follows.

$$An^4 - Bn^2 + C = 0 \tag{2.26}$$

$$A = Ssin^2\theta + Pcos^2\theta \tag{2.27}$$

$$B = RLsin^2\theta + PS(1 + cos^2\theta) \tag{2.28}$$

$$C = PRL \tag{2.29}$$

Eq. 2.26 is called the cold plasma dispersion relation. This relation gives 2 solutions of n^2 which determines the wave characteristics that can propagate in a cold plasma. Conditions that lead to the solution of Eq. 2.26 to $n^2 \to \infty$ are called resonance conditions, where conditions leading to $n = 0$ are called cutoff conditions. Since this equation's solutions behave differently at various propagation angles, which are typically unknown to experimentalists, a more useful formulation is required. Rewriting Eq. 2.26 in terms of the perpendicular refractive index given as $n_\perp^2 = n^2 sin^2\theta$ allows formulating the problem in terms of parameters that are typically known to experimentalists like the axial wave-number which is primarily driven by the antenna geometry.

$$A_1 n_\perp^4 - B_1 n_\perp^2 + C_1 = 0 \tag{2.30}$$

$$A_1 = S \tag{2.31}$$

$$B_1 = RL + PS - n_z^2(P + S) \tag{2.32}$$

$$C_1 = P(n_z^2 - R)(n_z^2 - L) \tag{2.33}$$

With Eq. 2.30 we can now understand the perpendicular propagation characteristics of the wave that has an axial wave-number driven by the antenna geometry we've designed. The perpendicular wave-number solved for by Eq. 2.30 is typically complex, the real part of this gives the perpendicular wavelength of the propagating wave while the imaginary part gives the damping length of the propagating wave. However, as discussed in Section 2.2 to estimate power coupling with the cold plasma approximation one must employ an effective mass term.

Phase Velocity

An important concept in plasma wave physics that can be understood from the propagation characteristics determined by the dispersion relationship is the phase velocity of the wave. A description and derivation of

the phase velocity can be found in [28] and the equation describing it is presented below.

$$\vec{v}_p = \omega \frac{\vec{k}}{|k|^2} \tag{2.34}$$

The magnitude of the phase velocity characterizes the speed at which points of constant phase on the wave. These points of constant phase travel in the direction of the wave-vector. This phase velocity relevant for understanding kinetic damping such as Landau and cyclotron damping, but also is useful concept in understanding wave patterns from wave-field measurements and simulations.

Group Velocity

The phase velocity however does not give us an understanding of the propagation of power in the plasma. The group velocity is the quantity that predicts the direction of the Poynting vector in the plasma, or the direction of energy propagation. Unlike for the vacuum case the direction of the phase velocity and the group velocity in a plasma is not the same. A derivation of the group velocity is found in [28] and the result of that derivation is shown here.

$$\vec{v}_g = \nabla_k \omega(k) \tag{2.35}$$

The direction of the group velocity is useful to understand if one wants to know how the energy from the antenna then propagates into the plasma. Defining the wave-vector in terms of its magnitude and direction from the magnetic field $\vec{k} = k(sin\theta\hat{\perp} + cos\theta\hat{z})$ we derive an expression for the angle of the group velocity with respect to the magnetic field (α) and write the expression below.

$$tan\alpha = -\frac{1}{k}\frac{\partial k}{\partial \theta} \tag{2.36}$$

From α we can now understand the direction the energy propagates with respect to the DC magnetic field. With an understanding of this direction and a damping length we can estimate how much wave power can reach the core of the plasma from an antenna.

2.2 Power Coupling

The cold plasma dielectric tensor does not predict a power deposition mechanism on its own. In fact there are no absorption mechanisms present in the form given by Eq. 4.17. To calculate a power absorption

mechanism one can modify the derivation of the STIX tensor to include power deposition mechanisms. In the conditions of the Proto-MPEX plasma we will only consider collisional absorption of the waves since the plasma conditions are very collisional which reduces the mean free path such that kinetic effects in the plasma are unlikely to occur.

2.2.1 Collisional Absorption

Collisional absorption in a cold plasma derivation can be accounted for by the Krook model which is considered by modifying the collision term, $\left(\frac{\partial f}{\partial t}\right)_{coll}$, in the Boltzman equation describing the evolution of the distribution function, $f(\vec{r},\vec{v},t)$, for charged particles as:

$$\frac{\partial f}{\partial t} + \vec{v} \bullet \nabla f + \frac{q}{m}(\vec{E} + \vec{v} \times \vec{B}) \bullet \nabla_v f = \left(\frac{\partial f}{\partial t}\right)_{coll} \tag{2.37}$$

The Krook model then assumes that the form of the collision term is given as:

$$\left(\frac{\partial f}{\partial t}\right)_{coll} = -\nu f_1 = -\nu(f - f_0) \tag{2.38}$$

$$f_0(\vec{r},\vec{v}) = Ae^{-E/kT} \tag{2.39}$$

In Eq. 2.39 the equilibrium distribution function is given by a Mawellian distribution. E is the sum of the potential and kinetic energy of the particle, A is a normalization constant, k is the Boltzmann constant, T is the thermodynamic temperature, ν is the collision frequency, and f_1 is the perturbed distribution function. Taking the first moment of the distribution function by averaging Eq. 2.37 in velocity to revive the momentum equation then yields.

$$\rho_j \left(\frac{\partial \vec{v}_j}{\partial t} + \vec{v}_j \bullet \nabla \vec{v}_j\right) = -qn_e(\vec{E} + \vec{v_j} \times \vec{B}) - \nabla p_j - \rho_j \vec{v}_j \nu \tag{2.40}$$

Fourier transforming Eq. 2.40 and rearranging terms gives.

$$(\nu + i\omega)(\rho \vec{v}_j) = -qn_r(\vec{E} + \vec{v}_e \times \vec{B}) - \nabla p_e \tag{2.41}$$

This result shows that the collisions interrupt the particle momentum. This momentum interruption can be accounted for in the cold plasma theory by replacing all the ω terms that came from the equations of motion in the STIX tensor by $\omega \rightarrow (\omega + i\nu)$. This is more easily accomplished by replacing the mass terms in Eq. 4.17 with $m_{j_{effective}} \equiv m_j(1 + i\frac{\nu}{\omega})$.

2.3 Collisions

The collisional processes in a plasma are important and govern many aspects of the plasma behavior. Collisions in a plasma will appear in the continuity, momentum balance, and power balance. In the parameter space of cold, high density plasmas the collisions will govern the macroscopic behavior of the plasma. As described in Section 2.2 collisions will also govern RF power deposition in a cold plasma. It is therefore important to understand the dominant collisional processes in the plasma under investigation.

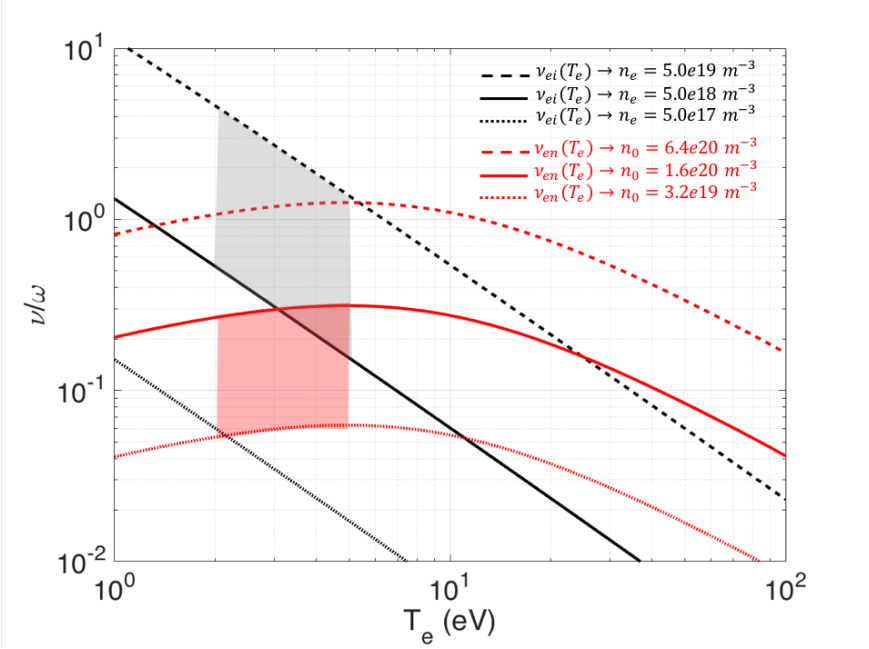

Figure 2.1: The black lines show normalized electron ion Coulomb collision frequency (ν_{ei}) plotted as a function of T_e for 3 different values of electron density ($n_e = 5.0e17\ m^{-3}$ (dotted), $n_e = 5.0e18\ m^{-3}$ (solid), $n_e = 5.0e19\ m^{-3}$(dashed)). The red lines show normalized electron neutral collision frequency (ν_{en}) plotted as a function of T_e for 3 different values of Deuterium density ($n_0 = 3.2e19\ m^{-3}$ (dotted), $n_0 = 1.6e20\ m^{-3}$ (solid), $n_0 = 6.4e20\ m^{-3}$(dashed)). The collision frequencies are all normalized to the driving frequency of the antenna ($\omega = (2\pi)13.56MHz$). The red shaded region denotes the expected parameter space of electron neutral collision frequency in Proto-MPEX. The grey shaded region denotes the expected parameter space of electron ion collision frequency.

In Proto-MPEX the region directly under the helicon antenna is poorly diagnosed due to the complications of making measurements in this region (probe and optical access, plasma is perturbation by probe

measurements, strong RF fluctuations), and therefore much speculation is typically involved when interpreting the measurements made in this area. However, the measurements indicate that the plasma created by the helicon antenna on Proto-MPEX is a relatively cold ($T_e \approx 2-5\ eV$) and dense plasma ($n_e \approx 1\times10^{18}$ (edge) 5×10^{19} (core) m^{-3}). The neutral gas density in this region can be approximated by baratron measurements on either side of the helicon antenna. However, it is important to understand that the baratron measurement is only representative of the edge density in Proto-MPEX, the core plasma is estimated to be close to 100% ionized. This can be shown by Abel inversions of the D_α light emission profiles from a fast frame camera which shows a hollow emission profile. The shaded regions in Fig. 2.1 shows the expected collision frequency in Proto-MPEX's parameter range, from this we can see that 1) Coulomb collisions dominate the collisional processes in the core plasma 2) an estimated average collision frequency is taken to be $\nu = \omega$. Fig. 2.1 shows the calculation of collision frequency for electron ion Coulomb collisions as well as electron neutral collisions. The following subsection will go over the details of these calculations. A summary on collisional processes in plasmas can be found in [29].

2.3.1 Electron Neutral Collisions

The calculation of the electron neutral collision frequency will be presented in this subsection. The collision frequency for electron neutral collisions is calculated by averaging the velocity dependant cross section over the velocity distribution of the electrons in the plasma. The energy dependant cross section for elastic collisions can be found on LxCat database online [30].

$$\nu_{en} = < \sigma_{en} v_e > n_0 \tag{2.42}$$

$$< \sigma_{en} v_e > = \int \sigma_{en}(v) f(v) dv \tag{2.43}$$

Where ν_{en} is the electron neutral collision frequency, $< \sigma_{en} v_e >$ is the reaction rate, n_0 is the neutral gas density, and $f(v)$ is the velocity distribution of electrons which is taken to be Maxwellian distribution with an electron temperature T_e.

2.3.2 Coulomb Collisions

The lengthy derivation of Coulomb collisions can be found in [29]. The analytical treatment to obtain the Coulomb collision frequency requires to calculate the cross section for a 90-degree deflection of a particle trajectory by integrating over many single small-angle collisions. Throughout this subsection the equations

used for calculating the Coulomb collision frequencies will be presented. Writing the equations of a reduced mass for a particle is written:

$$m_{rij} = \frac{m_i m_j}{m_i + m_j} \tag{2.44}$$

For the case of the derivation $i, j = e, i$ representing either electron or ion mass. Next we write the definitions for the Coulomb logarithm's used.

$$ln(A_{ei}) = log\left(\frac{\lambda_D}{q^2/(4\pi\epsilon_0 m_{rei} v_{the}^2)}\right) \tag{2.45}$$

$$ln(A_{ee}) = log\left(\frac{\lambda_D}{q^2/(4\pi\epsilon_0 m_{ree} v_{the}^2)}\right) \tag{2.46}$$

$$ln(A_{ii}) = log\left(\frac{\lambda_D}{q^2/(4\pi\epsilon_0 m_{rii} v_{thi}^2)}\right) \tag{2.47}$$

In Eq. 2.45 through 2.47 v_{the} is the electron thermal speed, v_{thi} is the ion thermal speed, and λ_D is the plasma Debye length. The equations for the Coulomb collision frequencies can now be written as:

$$\nu_{ei} = \frac{2}{3\sqrt{2\pi}} \frac{n_e Z^2 q^4}{(4\pi\epsilon_0)^2} \frac{4\pi}{\sqrt{m_e T_e^3}} ln(A_{ei}) \tag{2.48}$$

$$\nu_{ee} = \frac{1}{3\sqrt{pi}} \frac{n_e q^4}{(4\pi\epsilon_0)^2} \frac{4\pi}{\sqrt{m_e T_e^3}} ln(A_{ee}) \tag{2.49}$$

$$\nu_{ie} = \frac{m_e}{m_i} \nu_{ei} \tag{2.50}$$

$$\nu_{ii} = \frac{1}{3\sqrt{pi}} \frac{n_e q^4}{(4\pi\epsilon_0)^2} \frac{4\pi}{\sqrt{m_i T_i^3}} ln(A_{ii}) \tag{2.51}$$

Where Eq. 2.48 through 2.51 give the expressions for the collision frequency for electron-ion, electron-electron, ion-electron, and ion-ion collisions.

2.4 Bounded Wave Theory

In Section 2.1 the derivation of the cold plasma dielectric tensor and the dispersion relation in a homogeneous infinite plasma was presented. The following section will take into consideration geometric effects of a cylindrical cavity to derive a bounded dispersion relation. The derivation was originally presented in [17]

and the results are summarized below. The geometry considered here is a cylindrical conducting cavity of radius R and length L, filled with homogeneous plasma of radius r_0. The plasma cavity is excited by a straight single-loop antenna at radius r_0.

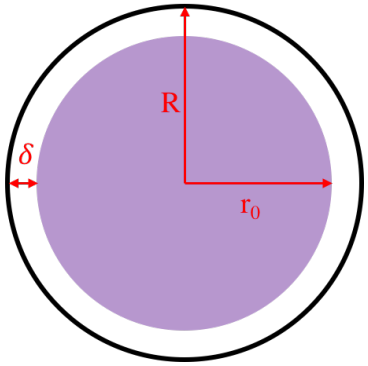

Figure 2.2: Schematic of a plasma column of radius r_0 separated from the electric conductor at radius R by a gap of δ.

Fig. 2.2 shows a schematic of the geometry considered below. This simple geometry is now used to derive bounded dispersion relations using the approximations of a whistler wave. The whistler dispersion is not entirely applicable to describe the wave in the conditions in Proto-MPEX, since the whistler dispersion ignores the ion cyclotron frequency which becomes important when operating near the high-density limit of the lower-hybrid resonance (HDLH).

2.4.1 Wave Fields in the Plasma Column

The fields in the plasma cavity are governed by Maxwell's equations given by Eq. 2.2 and 2.3, where the electric displacement field is now defined by $D = \overleftrightarrow{K} \bullet \vec{E}$. Ignoring the ion terms in the cold plasma tensor given by Eq. 4.17 through 2.20 simplifies the tensor components to:

$$P = \epsilon_{\parallel} = 1 - \frac{\omega_{pe}^2}{\omega(\omega + i\nu)} \tag{2.52}$$

$$S = \epsilon_{\perp} = \frac{(\omega + i\nu)\omega_{pe}^2}{\omega\Delta} \tag{2.53}$$

$$D = \epsilon_{\times} = \frac{\omega_{pe}^2\omega_{ce}}{\omega\Delta} \tag{2.54}$$

$$\Delta = (\omega + i\nu)^2 - \omega_{ce}^2 \tag{2.55}$$

The antenna current density and the wave fields are represented as a Fourier series in the axial, $k_z = l\pi/L(l = 1, 2, ...)$, and the azimuthal, $m = \pm 1, \pm 3, ...$,directions. With these assumptions the radial variation

of the electric field can be analytically expressed as:

$$E_{r_p} = A_{TG}\frac{1}{\alpha\beta}J'_m(k_{\perp_{TG}}r) + A_H\frac{1}{\beta}J'_m(k_{\perp_H}r) \tag{2.56}$$

$$-iE_{\phi_p} = A_{TG}\frac{m}{k_z r}J_m(k_{\perp_{TG}}r) + A_H\left(J'_m(k_{\perp_H}r) + \frac{m}{k_z r}J_m(k_{\perp_H}r)\right) \tag{2.57}$$

$$E_{z_p} = A_{TG}J_m(k_{\perp_{TG}}r) + \alpha A_H J_m(k_{\perp_H}r) \tag{2.58}$$

The radial variation of the magnetic field is analytically expressed as:

$$B_{r_p} = A_{TG}n_z\alpha\left(J'_m(k_{\perp_{TG}}r) + \frac{m}{k_z r}J_m(k_{\perp_{TG}}r)\right) - A_H n_z\left(J'_m(k_{\perp_H}r) + \frac{m}{k_z r}J_m(k_{\perp_H}r)\right) \tag{2.59}$$

$$-iB_{\phi_p} = -A_{TG}\frac{n_z}{\beta}J'_m(k_{\perp_{TG}}r) - A_H\frac{n_z}{\beta}J'_m(k_{\perp_H}r) \tag{2.60}$$

$$B_{z_p} = -A_{TG}\frac{n_z}{\beta}J_m(k_{\perp_{TG}}r) - A_H\frac{n_z}{\beta}J_m(k_{\perp_H}r) \tag{2.61}$$

Introduced here are the perpendicular wave number associated with the SW, $k_{\perp_{TG}}$, and the FW, $k_{\perp_H}$, as well as the dimensionless parameters, α and β. These parameters are defined bellow as:

$$\alpha = \frac{\omega_{pe}^2}{\omega_{ce}^2 n_z^2} \tag{2.62}$$

$$\beta = \frac{\omega\omega_{ce}n_z^2}{\omega_{pe}^2} \tag{2.63}$$

$$k_{\perp_{TG}} = k_z\frac{\omega}{(\omega + i\nu)\alpha\beta} \tag{2.64}$$

$$k_{\perp_H} = k_z\frac{1}{\beta}\left(1 + \frac{(\omega + i\nu)\alpha}{\omega}\right) \tag{2.65}$$

From the above equations it is clear that the wave-fields in the plasma are written as a superposition of the slow-wave and fast-wave in the plasma column with amplitudes given by A_{TG} and A_H respectively. $A_{TG,H}$ are defined in the later section and derived through applying the boundary conditions.

2.4.2 Wave Fields in the Vacuum Gap

Wave-fields in the vacuum layer, $R > r > r_0$, are described as a superposition of cylindrical TE and TM modes. The electric field in the vacuum layer is given bellow:

$$E_{r_v} = A_{TM}\Delta_{10} + A_{TE}\frac{m}{n_z k_z r}\Delta_{01} \tag{2.66}$$

$$-iE_{\phi_v} = A_{TM}\frac{m}{k_z r}\Delta_{00} + A_{TE}\frac{1}{n_z}\Delta_{01} \tag{2.67}$$

$$E_{z_v} = A_{TM}\Delta_{00} \tag{2.68}$$

The magnetic field in the vacuum layer is given bellow:

$$B_{r_v} = -A_{TM}\frac{m}{n_z k_z r}\Delta_{00} - A_{TE}\frac{m}{k_z r}\Delta_{11} \tag{2.69}$$

$$-iB_{\phi_v} = -A_{TM}\frac{1}{n_z}\Delta_{10} - A_{TE}\frac{m}{k_z r}\Delta_{01} \tag{2.70}$$

$$B_{z_v} = A_{TE}\Delta_{01} \tag{2.71}$$

The radial variation as a function of the radius of the electrical conductor is capture in the following functions:

$$\Delta_{00}(r,R) = I_m(k_z r) - \frac{K_m(k_z r)I_m(k_z R)}{K_m(k_z R)} \tag{2.72}$$

$$\Delta_{01}(r,R) = I_m(k_z r) - \frac{K_m(k_z r)I'_m(k_z R)}{K'_m(k_z R)} \tag{2.73}$$

$$\Delta_{10}(r,R) = I'_m(k_z r) - \frac{K'_m(k_z r)I_m(k_z R)}{K_m(k_z R)} \tag{2.74}$$

$$\Delta_{11}(r,R) = I'_m(k_z r) - \frac{K'_m(k_z r)I'_m(k_z R)}{K'_m(k_z R)} \tag{2.75}$$

2.4.3 Boundary Conditions

Joining the vacuum and plasma fields at the boundary ($r = r_0$) requires satisfying the boundary condition for the tangential electric and magnetic fields. The boundary condition for the the tangential electric field being continuous across the boundary is then written as:

$$E_{\phi,z_v} = E_{\phi,z_p} \tag{2.76}$$

The boundary condition for the discontinuity of the magnetic field across this boundary due to the

antenna current is written as:

$$B_{\phi,z_v} - B_{\phi,z_p} = -i\frac{mn_z}{k_z r} I \tag{2.77}$$

With the boundary conditions given by Eq. 2.76 and 2.77 the constants A_{TG}, A_H, A_{TE}, and A_{TM} are now defined. This joining completes the problem of a linear response of the plasma cavity to the external antenna.

2.4.4 Bounded Dispersion Relation

The joining procedure of applying Eq. 2.76 and 2.77 and solving for the constants related to the plasma fields yields the following relationship for these constants:

$$A_{TG} = \beta\frac{D_H}{D} I \tag{2.78}$$

$$A_H = -\beta\frac{D_{TG}}{D} I \tag{2.79}$$

Where the constants that define the amplitude of the SW and the FW are functions of the terms derived when solving for the eigenvalue problem, setting $I = 0$ in Eq. 2.77. These terms are given bellow:

$$D = -D_{TG}D_{TE} + D_H J_m(k_{\perp_{TG}} r_0) \tag{2.80}$$

$$D_{TG,H} = J'_m(k_{\perp_{TG,H}} r_0) + \frac{m}{k_z r_0} J_m(k_{\perp_{TG,H}} r_0) \tag{2.81}$$

$$D_{TE} = -\delta D_H + J_m(k_{\perp_H} r_0) \tag{2.82}$$

$$\delta = -\beta\frac{\Delta_{01}(r_0, R)}{\Delta_{11}(r_0, R)} \tag{2.83}$$

The result of the eigenvalue problem is retrieved when setting $D = 0$. This results in resonance behavior, and the constants $A_{TG,H}$, blow up to infinity. Resonance behavior however is only observed and clearly defined when the vacuum gap defined in the problem is very narrow. This can be expressed in the following expression:

$$\frac{R - r_0}{R} \ll \beta \frac{k_z R}{m^2 + k_z^2 R^2} \leq \frac{\beta}{2|m|} \tag{2.84}$$

Then the inequality $\delta \gg 1$ so one can approximate $D \approx D_{TG} D_H$ and retrieve separate resonant behavior of the SW and the FW inside of the cavity. However, in the situation of a wide vacuum gap in which the inequality $\frac{R-r_0}{R} > \frac{\beta}{2|m|}$ holds, the resonant behavior is a hybrid one because the SW and FW are strongly coupled. Inspecting Eq. 2.78 and 2.79 one can see that another behavior is present in this treatment of the problem. It is the anti-resonant behavior of the waves in the plasma cavity. The SW anti-resonance is given by setting $D_H = 0$ and the FW anti-resonance is given by setting $D_{TG} = 0$. This treatment now retrieves a bounded dispersion relation for the case of plasma cavity with a wide vacuum gap. The analytical treatment of a FW resonance and a SW anti-resonance gives the same dispersion relation given by $D_H = 0$.

2.5 Mode Conversion in Helicon Sources

Throughout this thesis the interplay between the cold plasma SW wave and the cold plasma FW wave will be discussed. A simple description of non-resonant mode conversion will be presented. Non-resonant mode conversion is thought to be the excitation mechanism for the SW at the periphery of the plasma that produces edge heating in helicon sources. A simple picture of resonant mode conversion of the SW to FW will also be discussed to point out the difference between this mode conversion and non-resonant mode conversion.

2.5.1 Slow Wave Excitation in Helicon Sources

Shamrai [22] discusses three mechanisms that the slow-wave is excited by in a helicon source. These mechanisms are 1) direct excitation by the RF antenna current 2) surface mode conversion (non-resonant) of the FW to the SW 3) bulk mode conversion (resonant) of the FW to the SW. The schematic shown in Fig. 2.3 shows a cartoon depicting 1) and 2).

Fig. 2.3 shows a cartoon schematic of the excitation mechanisms of the SW and a FW in a plasma column. The antenna near fields will excite both a propagating SW and FW. The SW's energy travels at a very shallow angle to the magnetic field, which typically restricts the power from direct excitation under the antenna to penetrate into the core plasma. The FW travels at a steep group velocity which allows the wave to reach the core plasma. However, the FW is typically weakly damped via collisions and Landau damping has been show to play a minor role in the power deposition of this wave [31]. In plasmas with modest

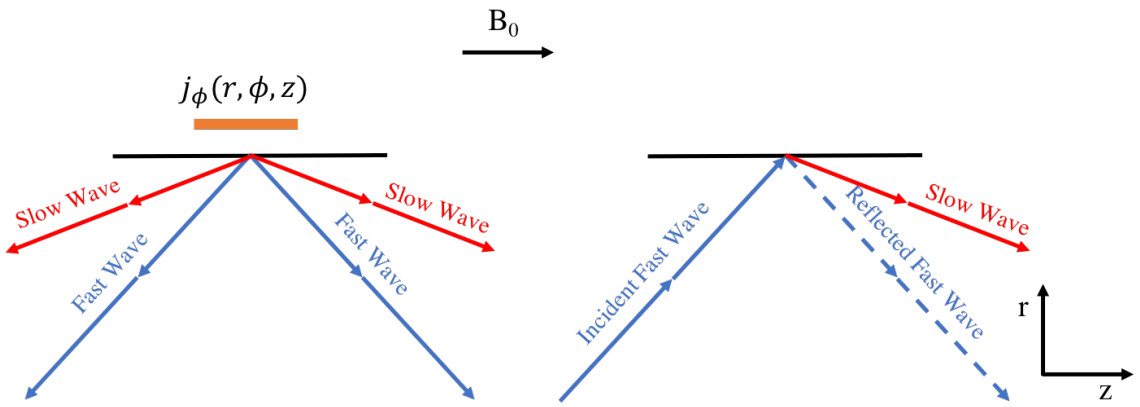

Figure 2.3: Schematic of slow wave excitation mechanisms in a helicon source. Left) slow wave excitation via direct excitation from the antenna current. Right) slow wave excitation via non-resonant mode conversion mechanism.

electron densities the collision frequency is orders of magnitude below the driving frequency and collisional damping does not play a large role in the power deposition of the wave. The non-resonant mode conversion arises from the FW reflecting from a sharp gradient in the index of refraction, such as an electron density gradient at the periphery of the plasma. Non-resonant mode conversion in helicon sources will described in more detail below.

2.5.2 Resonant Mode Conversion

Mode conversion of waves in plasmas has been studied in great mathematical rigor and more on this topic can be found in [32, 28]. In this section a simple picture of mode conversion will be presented. Mode conversion of one wave to another occurs at a region of space where the phase velocity and the polarization of both waves match. Fig. 2.4 shows the solutions of the dispersion relation of the FW and SW as a function of electron density. We see that along the electron density gradient the solutions meet at a $k_\perp$. In this region mode conversion of the FW to the SW could be expected. In helicon sources this type of mode conversion typically does not result in power transfer between the two wave branches.

2.5.3 Non-Resonant Mode Conversion

Shamrai [22] describes non-resonant mode conversion. The physical picture of non-resonant mode conversion is that an electron current that encounters a sharp gradient in electron density will produce a space charge upon reflection. The space charge produced gives rise to the excitation of the SW at the periphery of the plasma. The power associated with this type of mode conversion can be written as:

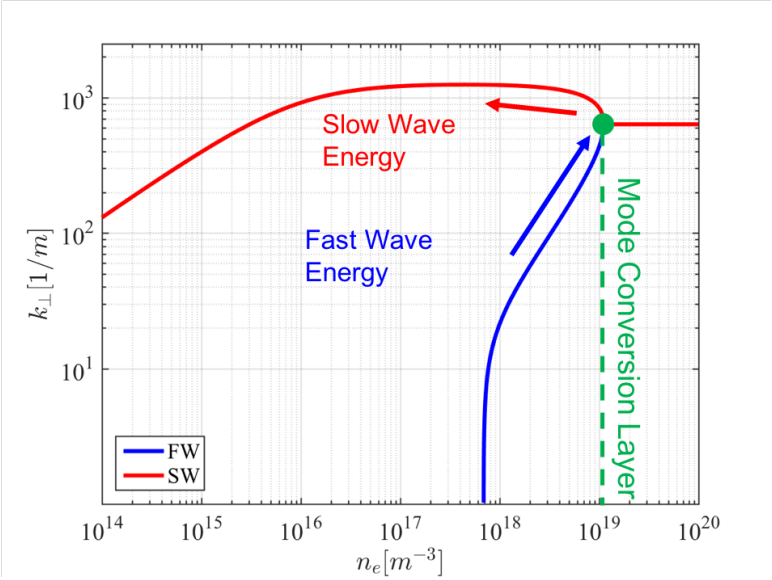

Figure 2.4: Resonant mode conversion schematic, the cold plasma dispersion relation is solved for an Argon plasma, with $B_0 = 300\ G$, $\omega = 13.56\ MHz$, $k_z = 20\ m^{-1}$, as a function of n_e. The fast wave branch (blue) and the slow wave branch (red) meet at an intermediate density of $n_e = 1 \times 10^{19}\ m^{-3}$ where the resonant mode conversion is expected to occur.

$$P_{conv} = \int E^{(SW)} \bullet J^{(FW)} dV \tag{2.85}$$

Where P_{conv} is the power transfered from the FW to the SW, $J^{(FW)}$ is the electron current associated with the propagating FW, and $E^{(SW)}$ is the electric field associated with the space charge produced by the reflecting current. Rewriting Eq. 2.85 to give a relationship between the wave amplitudes of the FW and SW gives:

$$|E_\theta^{(FW)}| = \frac{\omega}{\omega_{ce}} |E_r^{(SW)}| \tag{2.86}$$

Where $E_\theta^{(FW)}$ is the azimuthal electric field component of the SW, $E_r^{(SW)}$ is the radial electric field component of the SW.

Chapter 3

Experiment

This chapter will give an overview of the Proto-MPEX device. Section 3.1 will present a description of the helicon antenna used, the experimental parameters, magnetic field configuration and fueling recipes used. Next, section 3.2 will explain the diagnostics used for this work, mainly B-dot probes and IR thermography. Experimental observations will be presented in section 3.3. This section will present the trends of the electron density with magnetic field strength during the "helicon-mode". The heat flux measured at the target plate during a "helicon-mode" pulse will also be shown here and discussed. Finally, RF wave-field measurements made with the B-dot probes during "helicon-mode" operation will be discussed.

3.1 Proto-MPEX

In this section an overview of the Proto-MPEX device will be given. The helicon antenna used will be described here. Then, a description of the magnetic field configuration used for the data presented will be described. Finally, the gas fueling location and recipe will be presented.

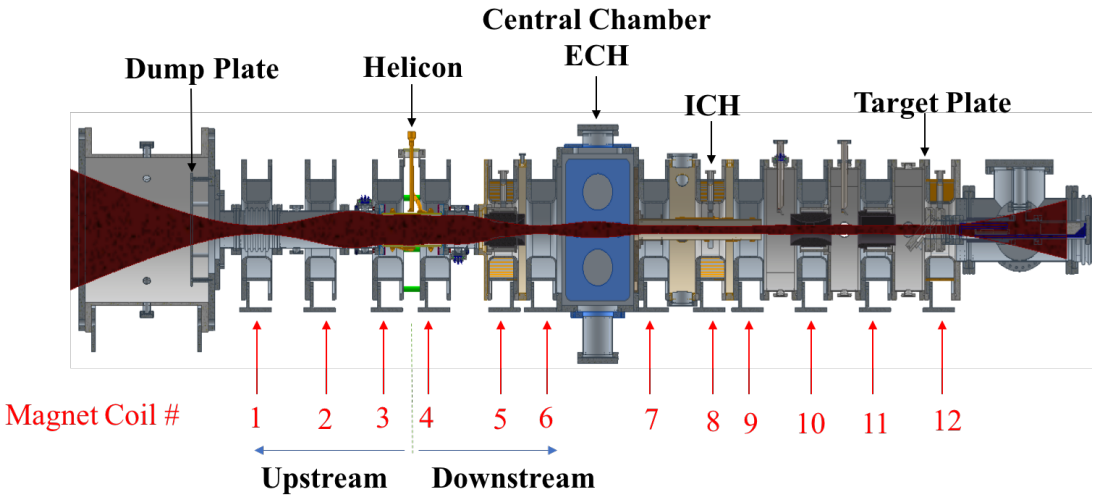

Figure 3.1: Schematic of Proto-MPEX showing the location of the helicon antenna, ECH launcher, and ICH antenna, dump plate, target plate, and magnetic coil configuration.

Fig. 3.1 shows the schematic of Proto-MPEX. The magnet coil geometry is shown and labeled here and will be referenced throughout this work to give the location of diagnostics and heating schemes. For example a Langmuir probe's location that is installed on the spool piece between magnet coils 9 and 10 will be referred to as "spool 9.5". The direction label of "upstream" will be given to the $-\hat{z}$ direction and "downstream" will be given to the $+\hat{z}$ direction. On the furthest downstream side of the device the plasma is terminated by a target plate and on the furthest upstream side of the device the plasma is terminated on a dump plate. The location of the helicon and ICH antennas as well as the ECH launcher is shown in this schematic as well.

3.1.1 Helicon Antenna

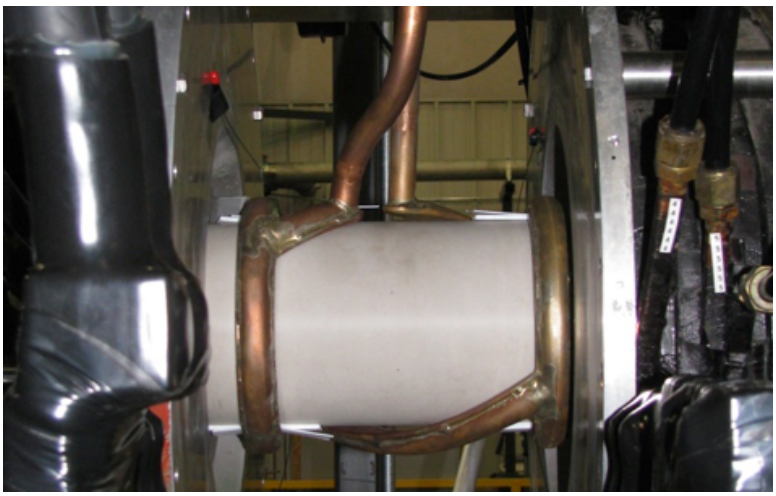

Figure 3.2: Picture of the Proto-MPEX helicon antenna installed.

Fig. 3.2 shows the helicon antenna installed on Proto-MPEX. The helicon antenna is a 25 cm helical right-handed quarter-turn antenna and is powered by $\geq$110 kW of RF power at 13.56 MHz frequency. The helicon antenna has a left-hand twist which primarily couples to the right-hand fast-wave; therefore, it is referred to as a right-hand antenna. The antenna is designed to be water cooled to run at steady-state on MPEX. It is located in air, and the vacuum "window" is an aluminum nitride (AIN) cylinder, chosen for it's thermal conductivity. Currently, the limiting factor in running the helicon antenna in steady-state is the heat load imposed on the vacuum window. A water cooled vacuum window has been designed and is being tested at the Controlled Shear Decorrelation Experiment (CSDX) located at the University of California San Diego.

3.1.2 Experimental Configuration

Throughout this work two main experimental configurations will be considered. On-axis magnetic field strength as well 2D flux mapping and device schematic are provided in Fig. 3.3 and 3.4 for Configurations A and B respectively. Configuration A was the first magnetic field and fueling configuration where the "helicon-mode" was observed and the results of those observations are published [23, 2]. Configuration B was then later established for electron heating experiments. Configuration B is advantageous to Configuration A for electron heating experiments in 2 ways; the magnetic geometry is predicted to allow better core electron heating and the fueling location allows for lower neutral pressure to be achieved in the central chamber which is essentially for wave heating of the electrons.

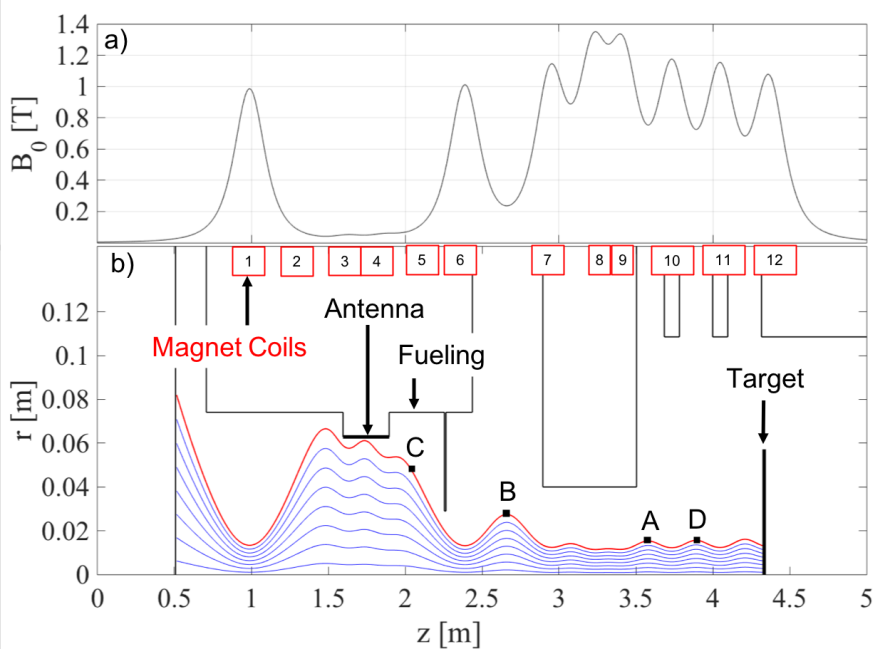

Figure 3.3: a) On-axis magnetic field strength in Proto-MPEX for Configuration A. b) Flux line mapping and two dimensional schematic of Proto-MPEX for Configuration A. The locations of the helicon antenna, gas fuelling, and locations of electron density measurements made with double Langmuir probes are shown and labeled.

Fig. 3.3 shows that the fueling location for Configuration A is 20 cm downstream of the helicon antenna. At this location Deuterium gas is injected at 8 equally space azimuthal locations. The Deuterium gas is injected at a flow rate of 2 standard liters per minute (SLM) 300 ms before the start of the RF pulse. At a time 50 ms before the RF power is turned on the gas flow is reduced to 0.5 SLM and 18 GHz mircowave power is applied to pre-ionize the gas. The 13.56 MHz RF pulse is then applied to the helicon antenna for 160 ms. The configuration that the magnets are run in is as follows; the mirror magnets (I_B) are coils 1, and 6-12, the supplemental magnets (I_0) are coils 2 and 5, and the helicon magnets (I_H) are coils 3 and 4.

The mirror magnets and supplemental magnets are held constant at $I_B = 5900$ A and $I_0 = 0$ A respectively. The helicon magnets are varied to control the field strength under the antenna.

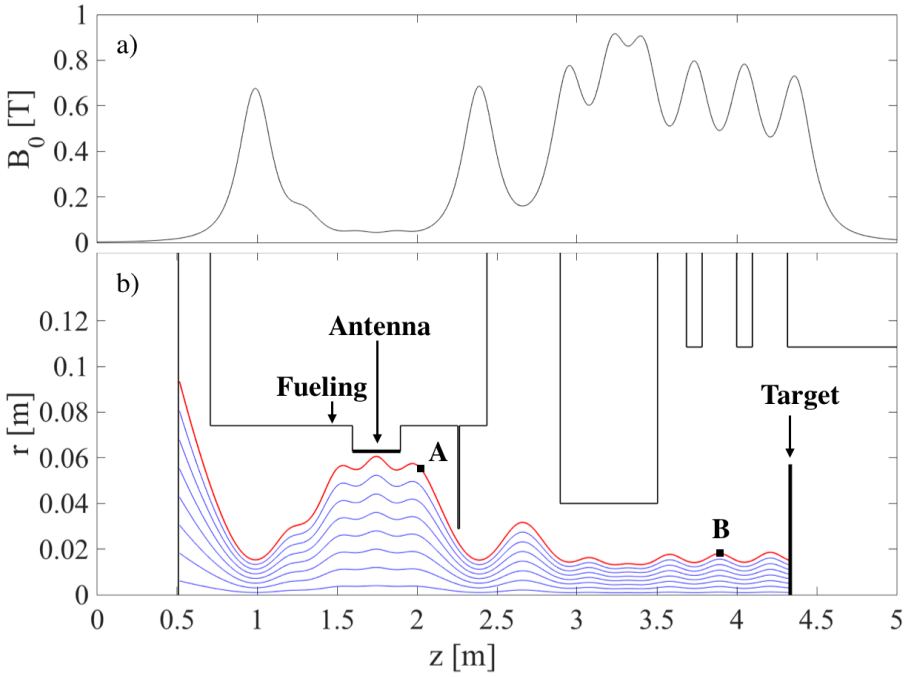

Figure 3.4: a) On-axis magnetic field strength in Proto-MPEX for Configuration B. b) Flux line mapping and two dimensional schematic of Proto-MPEX for Configuration B. The locations of the helicon antenna, gas fuelling, and locations of electron density measurements made with double Langmuir probes (A and B) as well as the location where B-dot probe measurements are made (B).

Fig. 3.4 shows that the fueling location for Configuration B is now moved to a location upstream of the helicon antenna. In this configuration the Deuterium gas is injected at a flow rate of 2.32 SLM 300 ms before the start of the RF pulse. At a time 50 ms before the RF power is turned on the gas flow is reduced to 0.8 SLM and 18 GHz mircowave power is applied to pre-ionize the gas. The 13.56 MHz RF pulse is then applied to the helicon antenna for 300 ms. The configuration that the magnets are run in is as follows; the mirror magnets (I_B) are still coils 1, and 6-12. The supplemental magnets from the previous configuration are now powered separately where coil 2 is powered with 600 A of current and coil 5 is turned off. The mirror magnets and helicon magnets are held constant at $I_B = 4500$ A and $I_0 = 160$ A respectively.

3.2 Diagnostics

The main diagnostics used throughout this work are double Langmuir probes, IR thermography, and B-dot probes. Throughout this section the design of the B-dot probes and the measuring circuitry as well as an

overview of the IR thermography diagnostic will be presented.

3.2.1 B-dot Probes

B-dot Probes were used to measure the phase and amplitude of the RF wave fields in Proto-MPEX in 2 axial locations near the helicon antenna. B-dot probes are a simple diagnostic that consist of a conducting coil used to measure time varying magnetic flux by exploiting Faraday's law of induction. When immersed in a time harmonic magnetic field a B-dot probe with a coil that with area A_e generates a voltage.

$$V = \omega B_1 A \tag{3.1}$$

Thus knowing the effective area of the coil and the operating frequency (ω) we can calculate the time harmonic magnetic field (B_1). Since the magnetic flux is a vector quantity the probe only picks up the vector component of the magnetic field that is pointing in the direction normal to the face of the coil. The B-dot probe constructed for Proto-MPEX consists of 2 coils orthogonal to each other, one directed radially and one that can be rotated to either measure the azimuthal or axial direction of $\vec{B_1}$.

Probe Design

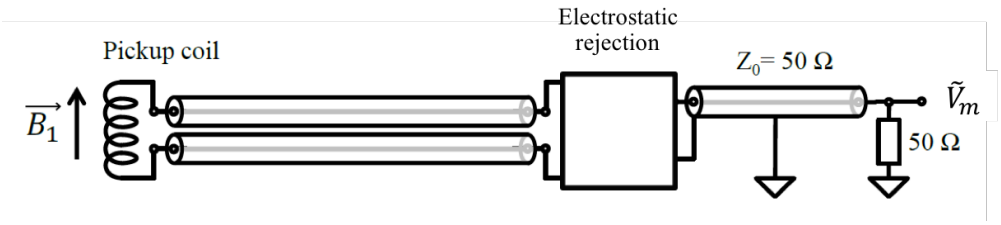

Figure 3.5: Schematic of the B-dot Probe used

The B-dot probe design is based on [33], and a schematic of the design is shown in Fig. 3.5. The signal wires are shielded by a custom coax that was constructed of hypodermic tubing and small diameter ceramic tubing. The electrical signals are brought outside of vacuum via 4 pin to BNC CF flange. Electrostatic rejection is achieved by connecting the signal wires to a 180° power splitter/combiner (ZMSCJ-2-1), the final signal should be a purely electromagnetic signal. This signal is then processed through measuring circuitry that digitizes only the amplitude and phase information of the 13.56 MHz signal, greatly reducing the amount of data that needs to be stored during the helicon pulse. The measuring circuitry is described in more detail below.

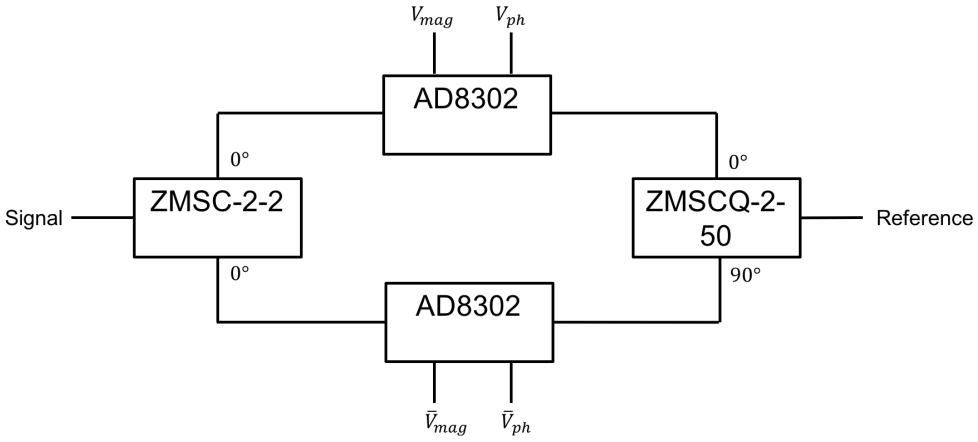

Figure 3.6: Schematic of the amplitude and phase detector used to process the B-dot probe signals

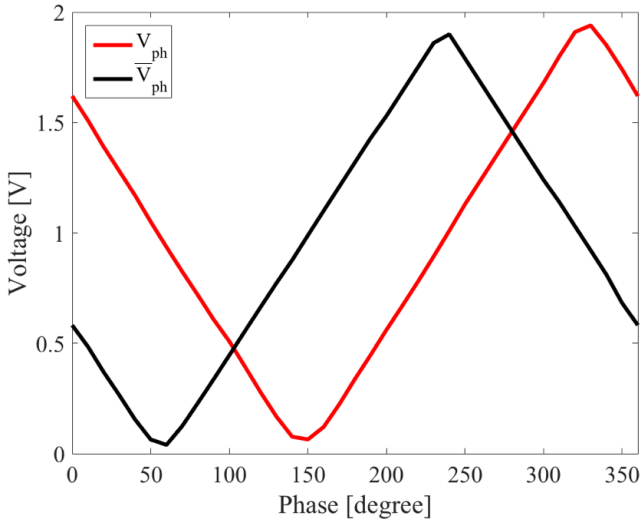

Figure 3.7: The voltage vs phase difference between the reference and signal.

Measuring Circuitry

After the electrostatic rejection the electric signal is processed by the amplitude and phase detector circuit shown in Fig. 3.6. The amplitude and phase detector circuit uses two AD8302 chips to resolve sign ambiguity of the phase and improve accuracy of the phase detector. There are 4 outputs from this phase and amplitude detector ($V_{ph}, \bar{V}_{ph}, V_{mag}, \bar{V}_{mag}$), however only 3 need to be digitized ($V_{ph}, \bar{V}_{ph}, V_{mag}$) since both magnitude voltages ($V_{mag}, \bar{V}_{mag}$) are the same value.

Fig. 3.7 shows the response of $V_{ph}, \bar{V}_{ph}$ when feeding the reference with a constant RF signal and varying the phase of the input signal. With only one AD8302 chip we would not be able to resolve the phase fully from 0 to 360 degrees. However with on of the AD8302 chips being fed with an input signal that is phase

shifted by 90 degrees we can resolve the full quadrant of the phase.

3.2.2 IR Thermography

Two-dimensional infra-red imaging of the target plate is performed using a FLIR A655sc IR camera, whose parameters are detailed in [34]. The frame rate of the IR camera is 50 Hz (0.02 s). The time scale on which this measurement is taken as well as the heat diffusion constant of the SS target allows ignoring radial and azimuthal heat diffusion within the target plate by satisfying $\frac{\partial T}{\partial t} \gg D(\nabla_\perp^2 T)$. Therefore, the time-differentiated thermal images give a two-dimensional profile of the plasma heat flux as determined by:

$$q_v = \rho c_p \frac{\partial T}{\partial t} \tag{3.2}$$

Where T is the temperature measured by the IR camera, c_p and ρ is the specific heat and density of the target plate, t is the time, q_v is the volumetric heat source which in the case of a plasma heat flux on the surface is written as $q_v(r,\phi,z) = q_s(r,\phi)\delta(z-z_0)$ where z_0 is the location of the target.

In the presence of strong magnetic fields it can be shown that radial electron heat transport can be neglected in comparison to axial heat transport. For typical Proto-MPEX plasma conditions it can be shown that for electrons $\frac{q_\parallel}{q_\perp} \gg \frac{L}{R}$, where $\frac{q_\parallel}{q_\perp} = \left(\frac{\omega_{ce}}{\nu_e}\right)^2 \frac{\nabla_\parallel T_e}{\nabla_\perp T_e}$ is the ratio of parallel to perpendicular electron heat flux [35]. The electron cyclotron frequency is ω_{ce}, ν_e is the electron collision frequency, T_e is the electron temperature, L is the length from the antenna to the target, and $R \approx 1$ mm is the characteristic radial scale of the measurement. Since the condition given above is satisfied, the plasma heat flux inferred from the IR emission profile on the target plate can be mapped back to the deposited heat upstream along the magnetic flux lines. This mapping is a good approximation of the origin of the power deposition.

3.3 Observations

Throughout this sections the experimental observations of the "helicon-mode" plasma is presented. First, observation of the electron density behavior with the magnetic field will be reported, and the behavior of the electron density radial profiles will be described. These observations where reported in [23] for Configuration A. Next, observations of the heat flux to the target are reported. Finally, the behavior of the RF fields during a "helicon-mode" plasma is described.

3.3.1 Electron Density and Temperature

The observations made here are were made with the device in configuration A. High-density operation of the helicon antenna on Proto-MPEX has been observed[2, 23] and is referred to as the "helicon-mode". This mode of operation was observed after experimentally optimizing gas fueling and the magnetic field profile.

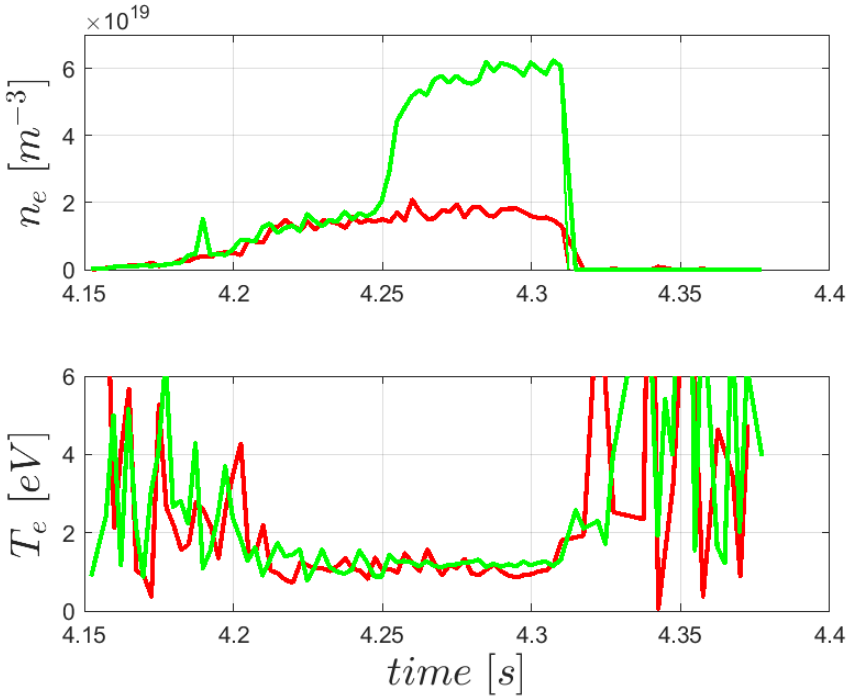

Figure 3.8: On-axis electron density (top) and temperature (bottom) evolution during a helicon pulse, for a pulse that "jumped" into the "helicon-mode" (shot 8574) and a pulse that did not (shot 8575). The plasma density and temperature is measured at the Location D shown in Fig. 3.3.

From Fig. 3.8 we can see that this mode of operation is characterized by an increase in on-axis electron density from 2×10^{19} to 6×10^{19} m^{-3}. This "jump" into the "helicon-mode" was observed 50 ms into the a 150 ms pulse. The electron temperature also decreases from 4 eV to ¡ 2 eV during the "helicon-mode".

From Fig. 3.9 we see that the transition from a hollow to centrally peaked electron density profile and transition from hollow to a flat electron temperature profile is observed during helicon mode. In Fig. 3.11 it is also observed that substantial increase in core power coupling as observed from IR thermography after the plasma is in the "helicon-mode". More details on the "helicon-mode" and its characteristics can be found in Ref. [23, 2]. The "helicon-mode" plasma is observed to be a stable plasma over the entire pulse length; recent experiments have been performed to extend pulse lengths to ¿ 1 s which showed a stable equilibrium plasma throughout the duration. Before the transition into the "helicon-mode" the plasma is noisy and low-frequency oscillations of electron density and temperature are observed on the double Langmuir probes,

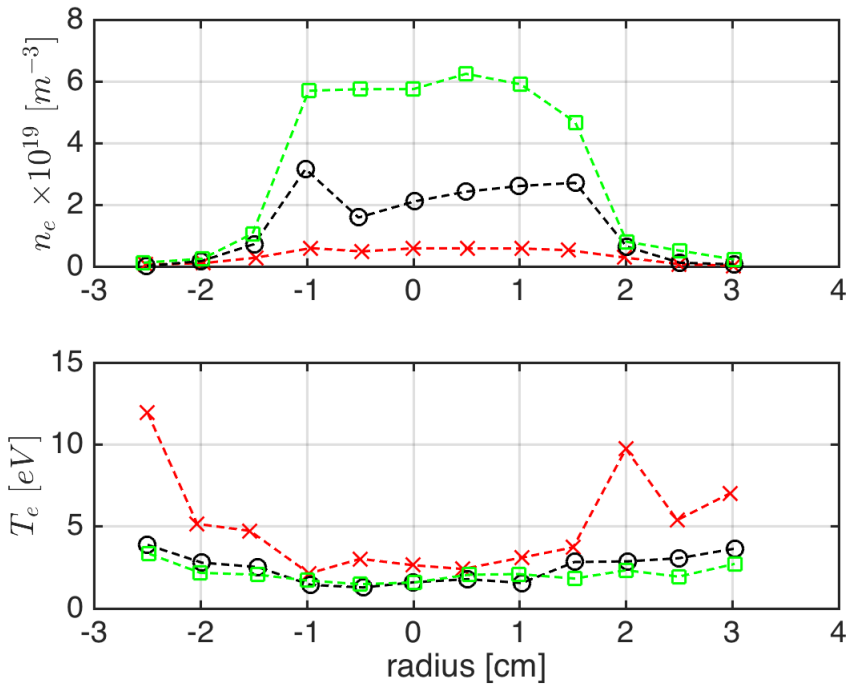

Figure 3.9: Radial scan of the electron density (top) and electron temperature (bottom), taken at different times for a helicon pulse that "jumped" into the helicon mode (shot 8574). The the measurements denoted by the red x's are taken between 4.17 to 4.20 s, the black circles are taken between 4.21 to 4.23 s, and the green squares are taken between 4.28 to 4.31 s. The plasma density is measured at the Location A shown in Fig. 3.3.

as is evident by Fig 3.8.

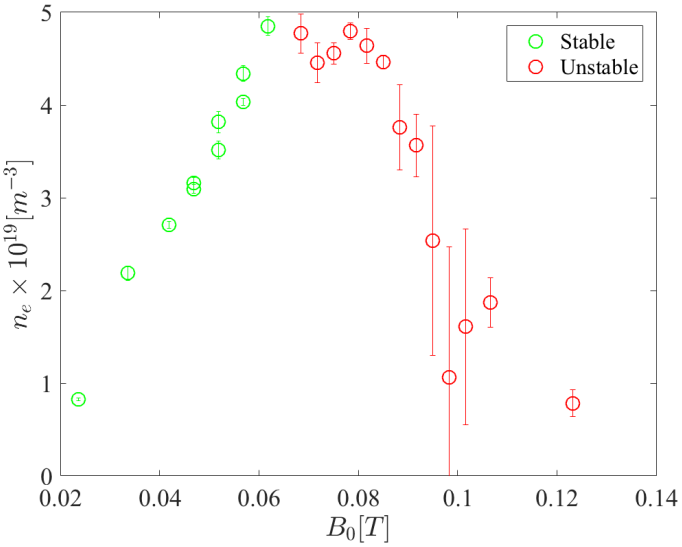

Figure 3.10: On-axis plasma density vs. magnetic field strength under the helicon antenna. The plasma density is measured at the Location A shown in Fig. 3.3.

Fig. 3.10 shows the results of scanning the magnetic field strength under the helicon antenna and measuring the electron density at Location A. It is observed that when the plasma is in "helicon-mode" there is a linear dependence of the electron density on the magnetic field. After $B_0 0.06$ T the electron density stagnates and eventually decreases. The plasma also becomes unstable at these higher magnetic field values as can be seen from the error bars in Fig. 3.10. The nature of these instabilities has not yet been explored in this device. However, the timescale of the instabilities is similar to those observed and characterized by Light[25]. Another possible source of the instability could be due to neutral depletion and the relaxation oscillations Degeling observed and described[36, 37]. Throughout this paper, the focus will be on characterizing the antenna coupling to the stable modes of the plasma. These modes exhibit a linear behavior of electron density with magnetic field strength as shown in Fig. 3.10.

3.3.2 Heat Flux

The heat flux measurements reported here were taken for experimental Configuration B. The heat flux to the target plate is shown in Fig. 3.11. The two-dimensional distribution of the heat fluxes at the start and end of the RF pulse are shown in panels (a) and (b) respectively. At the start (end) of the RF pulse, the heat flux is dominated by power deposition at the edge (core) of the plasma column. As is evident in panel (d), a transition is observed at approximately $t = 4.25\ s$ where the edge power deposition is suppressed and the core deposition begins to dominate. At the end of the pulse, the core power deposition is clearly dominant and delivers up to 0.6 $MWm^{-}2$ to the target plate. Extensive experimentation has shown that this edge-to-core transition can be reliable produced on demand provided that (a) the neutral gas is puffed at the location of the antenna about 300 ms before the RF pulse, (b) the neutral pressure before breakdown is 2-3 Pa and (c) the discharge is at least 100 ms in duration.

From a purely electromagnetic point of view, an important observation from the IR measurements in Fig. 3.11 is the suppression in edge power deposition in favour of core deposition. This suppression effect is predicted theoretically in [17] when discharge conditions allow the formation of normal modes of the fast-wave. This occurs analytically when Eq. 2.81 for the fast-wave equals 0. We can also conclude from these observations that the efficient plasma production in the Proto-MPEX helicon-mode is fast wave dominated since the dispersion relation doesn't allow the slow-wave to propagate in the high-density region where the power absorption is observed. The solution to the dispersion relation will be shown and discussed in Section 5.1.

The fast-wave is typically weakly damped by collisions and therefore collisional damping of the fast-wave typically does not contribute much to the power coupling in laboratory scaled helicon devices. However,

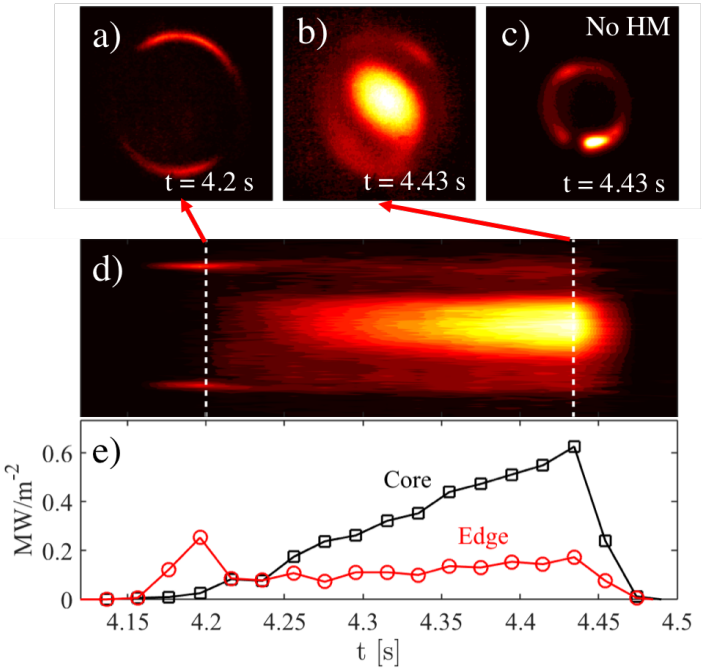

Figure 3.11: Heat flux to the target inferred from IR thermography (a) at the start of the RF pulse ($t = 4.2$ s) and (b) at the end of the RF pulse ($t = 4.43$ s). The length scale of the y and x axis is 4 cm across the image. Parts (a), (b), and (d) are the same discharge. Part (c) shows the end of the RF pulse ($t = 4.43$ s) in a condition where the discharge did not transition to core power deposition. Part (d) shows the time evolution of the heat flux to the target. Part (e) shows the time evolution of the heat flux to the target at the core (center of image) and at edge (location of largest heat flux at $t = 4.2$ s).

with the high electron density ($n_e > 10^{19}$ m^3) and low electron temperature ($T_e < 3$ eV) in this plasma a large collision frequency is expected ($\nu_e > \omega$) only accounting for Coulomb collisions. Several authors were able to explain the damping of the fast-wave in high density light-ion plasmas with a calculated collisional damping given by electron neutral and Coulomb collisions [14, 38].

3.3.3 RF Fields

The RF measurements presented here were made with the experiment in Configuration B. Presented in Fig. 3.12 is the magnitude of the B_r wave field component on-axis and at the edge of the discharge. At the same time as the transition from edge-to-core power deposition as seen in Fig. 3.11, the on-axis RF magnetic energy $|B_r|^2$ increases while the edge magnetic energy decreases. Fig.3.12 b) shows the RF pulse shape as well as on-axis electron density measurements at location A and B of Fig. 3.4. From this we can see that once the core heating is established, there is a correspondingly high plasma density at the source and the target location.

Fig. 3.13 presents a radial scan of the B_z component of the fast-wave measured at spool 4.5 during

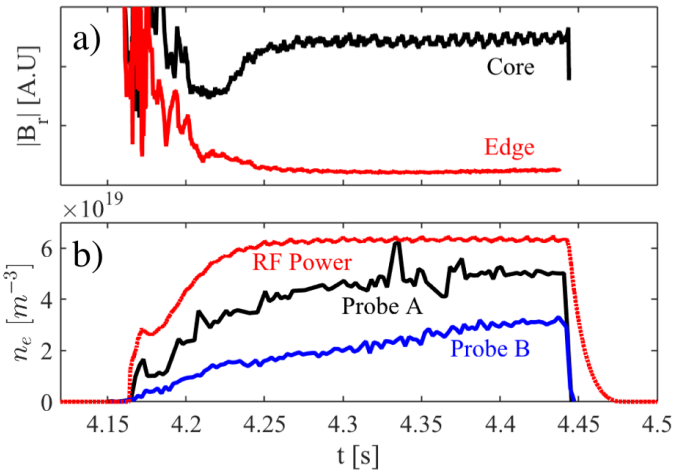

Figure 3.12: (a) B_r component of the fast-wave measured near the helicon antenna (location A) on-axis (black) and at the edge (red) of the plasma column. (b) On-axis plasma density measured at location A (black) and location B (blue). Red trace is the normalized RF power which peaks at $\approx$ 110 kW.

a core-heated discharge. The measurements in Fig. 3.13 indicate the formation of a radial normal-mode: (a) the radial variation of the magnitude displays the characteristic bimodal shape of the B_z ($m = +1$) component of the helicon mode and (b) the radial phase variation has the characteristic 180 degree phase shift on-axis. It is worth noting that before the edge-to-core transition or when this transition does not occur, both the amplitude and phase of the RF wave fields are strongly fluctuating and no clear indication of a radial normal-mode is observed.

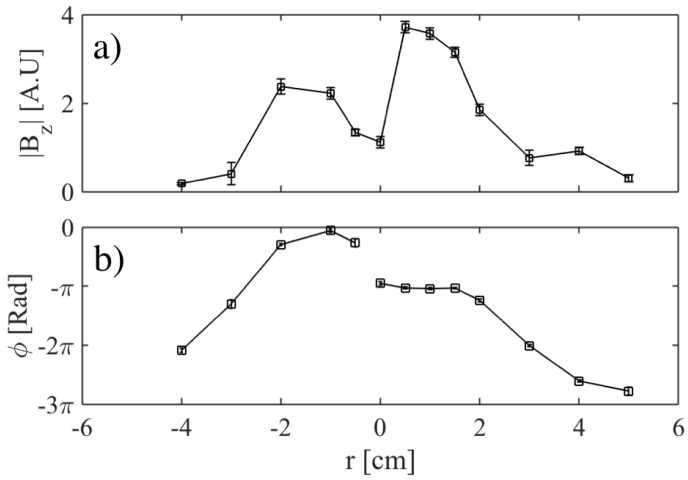

Figure 3.13: Radial variation of B_z measured with RF (B-dot) probe at location A at the end of a 150 ms RF pulse, (a) magnitude and (b) phase. The DC magnetic field at the source and target are 0.05 T and 0.6 T respectively, D_2 gas is injected at location A.

Fig. 3.11, 3.12, and 3.13 indicate that at the time of the increased core power coupling, measurements

performed at spool 4.5 (location A in Fig. 3.4) with B-dot probes indicate: (1) an increase in fast-wave energy density in the core plasma and (2) the formation of a fast-wave radial normal-modes. These experimental observation give evidence that the improved helicon-mode in Proto-MPEX is characterized by: (1) an increase in on-axis electron density up to $6 \times 10^{19}\ m^3$ at the source location, (2) significant core power coupling, (3) suppression of edge power coupling and (4) an increase in the fast-wave energy density in the core plasma due to the (4) formation of a fast-wave radial normal-modes. The self-consistent mechanism that drives the edge-to-core transition in Proto-MPEX is not yet understood; however, the transition displays characteristics that are consistent with the plasma column being in a slow-wave anti-resonance regime in steady state. This behavior of a helicon discharge is predicted by [17].

Chapter 4

Full Wave Model

This chapter will present the full wave models made in COMSOL multiphysics. Section 4.1 will give a description of the 3D helicon antenna model. The 3D model was mainly used to benchmark the antenna description used in the 2D model. The 2D axisymmetric model that was used to study the plasma physics is described in section 4.2. This section will go over the 2D antenna description, present the electron density profile used, and go over the tensor rotation implemented.

4.1 3D Helicon Antenna Model

This section will describe the 3D helicon antenna model. This model can also be used with the cold plasma tensor to investigate helicon physics and optimize engineering designs. However, the 3D model is more computationally intensive then the 2D axisymmetric model and presented difficulty resolving the slow-wave in a geometry large enough to study the Proto-MPEX configuration. Therefore, this model was mainly used to benchmark the analytical description of the 2D axisymmetric antenna. The current on the antenna is self consistently solved for in COMSOL after implementing a port boundary condition on the coaxial power input labeled in Fig 4.1.

Validation of the 2D axisymmetric antenna description was an essential step in developing a 2D axisymmetric model. The 2D antenna description must adequately capture the excited k_z spectrum. Higher k_z modes in the antenna near field spectrum would contribute to excitation of slow-waves in the edge of the plasma and overestimate the amount of power deposition in the edge relative to the core. The fast-wave is expected to significantly contribute to the density production in the Proto-MPEX helicon source when operating in the "helicon-mode" thus a proper description of the antenna current was an essential step for a model that represented the Proto-MPEX helicon source.

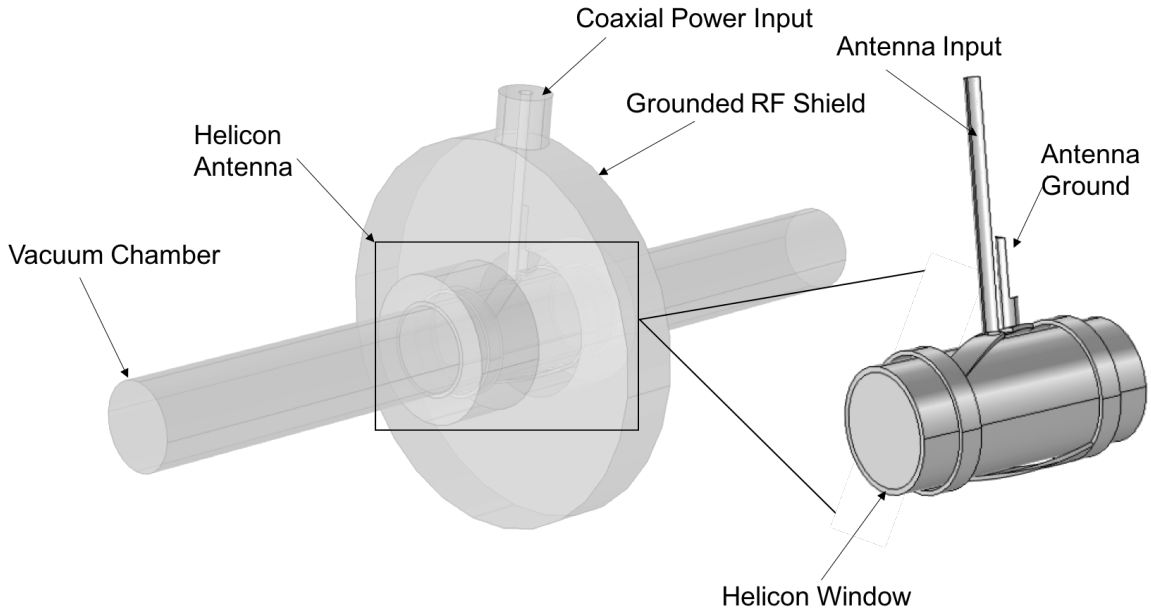

Figure 4.1: Schematic of the 3D helicon antenna model built in COMSOL Multiphysics. RF power is input in the form of a port boundary condition imposed on the Coaxial Power Input labeled and the antenna current on the helicon antenna is solved self consistently.

4.2 2D Asymmetric Model

Maxwell's equation is solved in the frequency domain using the finite element analysis software COMSOL Multiphysics.

$$\nabla \times \left(\nabla \times \vec{E} \right) - k_0^2 \overleftrightarrow{\epsilon_r} \vec{E} = 0 \tag{4.1}$$

A 2D axisymmetric geometry is used and the RF Electric field is solved for assuming $m = +1$ symmetry where the fields vary as $\vec{E}(r, \phi, z) = \bar{\vec{E}}(r, z)e^{-im\phi}$. The $m = +1$ mode is the dominant azimuthal mode that contributes to power deposition by right-handed helical antennas[39, 40] with a magnetic field oriented in $+\hat{z}$, therefore the paper will focus on the $m = +1$ azimuthal mode for the analysis of the plasma wave physics.

4.2.1 Antenna Description

The helicon antenna is described by a current imposed on a boundary at the radial location of the antenna. The current in physical space is described as a combination of the transverse current straps and the helical

strap of the antenna[41]. The component of the transverse current strap is given by Eq. 4.2.

$$J_{\phi}^{T} = \frac{I_0}{2}\left(R_1(u_{\phi 1} + u_{\phi 2}) + R_2(u_{\phi 3} + u_{\phi 4})\right) \tag{4.2}$$

The first term in Eq. 4.2 describes the current ring closer to the target, and the second term describes the current ring further from the target. The current rings are described as boxcar functions in the azimuthal coordinate ϕ and in the axial coordinate z.

$$R_1(z) = H\left(\frac{L_a}{2}, \frac{L_a}{2} - R_w\right) \tag{4.3}$$

$$R_2(z) = H\left(\frac{-L_a}{2} + R_w, -\frac{L_a}{2}\right) \tag{4.4}$$

$$u_{\phi 1} = +H(\theta, \theta + \pi) \tag{4.5}$$

$$u_{\phi 2} = -H(\theta - \pi, \theta) \tag{4.6}$$

$$u_{\phi 3} = +H(-\theta - \pi, -\theta) \tag{4.7}$$

$$u_{\phi 4} = -H(-\theta, -\theta + \pi) \tag{4.8}$$

The square function ($H(x)$) has properties such that:

$$H(a,b) = \begin{array}{ll} 1 & a < x < b \\ 0 & otherwise \end{array} \tag{4.9}$$

The azimuthal Fourier transform of the transverse and helical current straps is then given by:

$$\bar{J}_{\phi}^{T} = \frac{I_0}{2}\frac{4i}{m\sqrt{2\pi}}\left(-R_1 e^{-im\theta} + R_2 e^{im\theta}\right) \tag{4.10}$$

$$\bar{J}_{\phi}^{H} = 2\theta\frac{I_0}{L_a}\sqrt{\frac{2}{\pi}}e^{\frac{2im\theta z_a}{L_a}} \tag{4.11}$$

The total azimuthal current of the antenna is then given by the contribution from the helical strap and the two transverse straps. To define the axial current of the helical strap we can use the divergence-free condition ($\nabla \bullet \vec{J} = 0$) which results in the following definition for the axial current.

$$\bar{J}_z = -\frac{im}{R}\int \bar{J}_\phi^H dz \tag{4.12}$$

This integration then yields:

$$\bar{J}_z = -\frac{I_0}{R}\sqrt{\frac{2}{\pi}}e^{\frac{2im\theta z_a}{L_a}} \tag{4.13}$$

Eqs. (4.10),(4.11) and (4.13) are then used in the 2D axisymmetric simulation to describe the antenna. The vacuum spectrum of the antenna from the 2D simulation with both $m = \pm 1$ modes was compared to a COMSOL 3D simulation with real antenna geometry and a self-consistent antenna current. Fig. 4.2 shows the comparison of the vacuum spectra from the 2D and 3D simulations. In the 2D simulation, a damping term was added in the region where the antenna current was defined for numerical stability of the solution. However, this should not affect the results reported herein as the square of the field amplitude will scale linearly with increasing power and the field profiles are not affected by the amplitude of the fields.

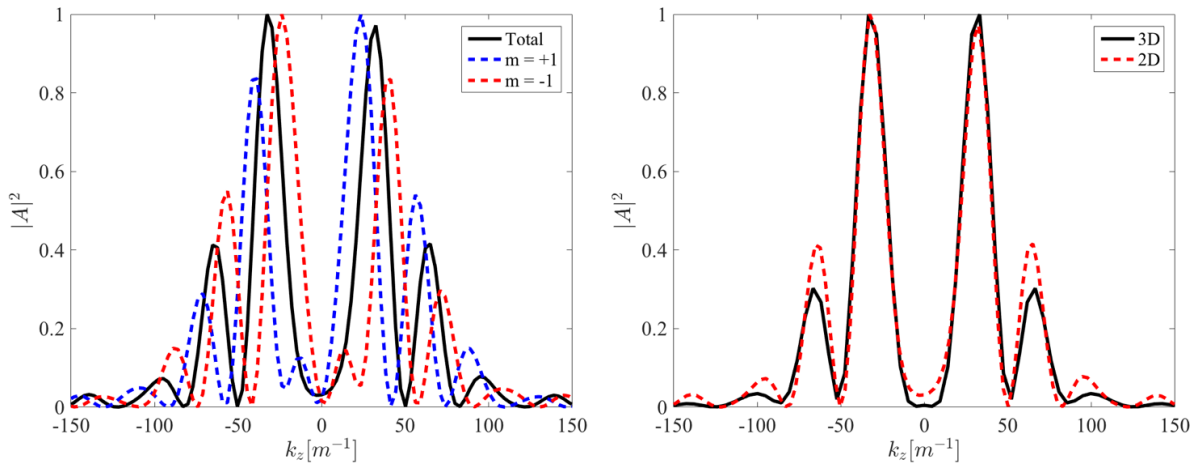

Figure 4.2: Fourier components of the vacuum B_z from the 2D axisymmetric simulation (Right). Comparison of the Fourier components of the vacuum B_z from the 2D axisymmetric simulation using the summed $m = +1$ and $m = -1$ modes of the antenna spectrum with a 3D self-consistent simulation of the helicon antenna (Left).

4.2.2 Electron Density Description

The model geometry represents a 2D axisymmetric slice of Proto-MPEX. The magnetic field geometry is modeled by solving Amperes law from the geometry and current configuration of the magnetic field coils.

The density is then implemented as a function of the radial coordinate and the azimuthal component of the magnetic vector potential ($A_\phi r$) whose contours correspond to the magnetic field lines in the geometry. The limiting flux line ($A_{\phi_{LF}} r$) is defined by the smallest value of the magnetic flux that intersects the chamber wall near the helicon region. The electron density is then defined as a function of χ.

$$n_e = \begin{cases} n_{e_{peak}} \left(1 - \chi^a\right)^b + n_{e_{edge}} & \chi \leq 1 \\ n_{e_{edge}} & \chi > 1 \end{cases} \tag{4.14}$$

$$\chi = \frac{A_\phi r}{A_{\phi_{LF}} r} \tag{4.15}$$

The peak electron density ($n_{e_{peak}}$) and the current imposed on the helicon magnet coils (I_H) is scanned over experimentally relevant conditions while the edge density is held constant at $n_{e_{edge}} = 10^{16}\ m^{-3}$ throughout the analysis. The constants controlling the density profile in Eq. (4.14) are set to $a = 2$ and $b = 1.75$. Fig. 4.3 shows Eq. (4.14) plotted against experimentally measured radial scans of electron density profiles measured at location A, B, and C. The experimental radial scans are converted to the χ coordinate based on calculated A_ϕ. The electron density is normalized to a peak density value in each measurement set. Axial variation of ($n_{e_{peak}}$) is not imposed since it is not clear how this varies in the experiment. This density profile replicates the variation of the plasma radius throughout the axial length of the device.

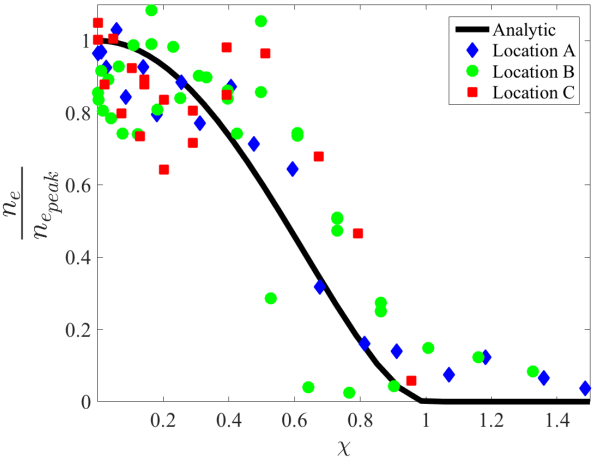

Figure 4.3: Normalized experimentally measured radial scans of electron density at location A, B, and C vs the electron density profile given by Eq. (4.14) with $a = 2$, $b = 1.75$, and $n_{e_{peak}} = 1$. The radius of the experimentally measured radial scans is converted to χ coordinate by multiplying by calculated A_ϕ.

4.2.3 Tensor Rotation

The plasma is represented as a dielectric tensor ($\overleftrightarrow{\epsilon_r}$) derived from cold plasma theory[28] assuming $\vec{B_0} = B_0\hat{z}$, this assumption is not valid in the Proto-MPEX magnetic geometry where strong gradients in the magnetic field result in significant curvature of the field lines. This is accounted for by rotating the dielectric tensor to the orientation of the magnetic field lines using the rotation matrix ($\overleftrightarrow{Q}$) to rotate the STIX tensor ($\overleftrightarrow{K}$) by the angle (Ψ) between the magnetic field and the axial coordinate $\hat{z}$.

$$\overleftrightarrow{\epsilon_r} = \overleftrightarrow{Q}_\phi \overleftrightarrow{K} \overleftrightarrow{Q}_\phi^T \tag{4.16}$$

$$\overleftrightarrow{K} = \begin{bmatrix} S & -iD & 0 \\ iD & S & 0 \\ 0 & 0 & P \end{bmatrix} \tag{4.17}$$

$$\overleftrightarrow{Q}_\phi = \begin{bmatrix} cos(\Psi) & 0 & sin(\Psi) \\ 0 & 1 & 0 \\ -sin(\Psi) & 0 & cos(\Psi) \end{bmatrix} \tag{4.18}$$

$$\Psi = tan^{-1}\left(\frac{B_r}{B_z}\right) \tag{4.19}$$

Damping of the wave is approximated by the Krook model[28] which is implemented by a collision frequency ν modifying the mass of the electrons as $m_{e_{eff}} = m_e\left(1 - i\frac{\nu}{\omega}\right)$. The effect of ν on the eigenmodes is discussed in section 5.2 of this paper.

Chapter 5

Simulation Results

Throughout this chapter the results from the Full Wave Model described in Chapter 4 will be presented. In section 5.1 dispersion relation calculations pertaining to the parameter space of the helicon antenna on Proto-MPEX will be presented. The dispersion calculations estimate the propagation characteristics of the waves in the full wave calculations, and are an important step in interpreting results from these calculations. In section 5.2 a parameter scan of peak electron density and magnetic field strength is performed and core power deposition is tracked as a figure of merit. The physics that gives rise to these contours of core power deposition is discussed in this section and the effect of collision frequency is presented. In section 5.3 the RF fields of simulations with a maximum and a minimum in core power deposition are compared. Finally, in section 5.4 the power deposition profiles of these two simulations are compared.

5.1 Dispersion Relation

Understanding the propagation characteristics predicted by the dispersion relation is essential when interpreting the results of an electromagnetic simulation. The helicon antenna installed on Proto-MPEX is installed on the outer edge of the plasma column and typically excites waves with k_z imposed by the antenna structure. Therefore, once the vacuum k_z spectrum of the helicon antenna is understood, Eq. 2.30 can be solved for $n_\perp$ to understand the expected wave behavior in the simulation. The following subsections will go over the solutions of the dispersion relation in Proto-MPEX conditions assuming $k_z = 20\ m^{-1}$, value of the highest peak from Fig. 4.2. First the effect of ion mass on the solutions of the dispersion relation will be shown in Fig. 5.1. Next the dispersion relation calculation for parameters measured at spool 4.5 will be shown. Finally a 2D contour of the fast-wave cutoff and lower hybrid resonance for a simulation using $n_{e_{peak}} = 2.7 \times 10^{19}\ m^3$ and $I_H = 260$ A will be shown.

5.1.1 Light Ion Helicon Dispersion

Sakawa[24] showed that for a helicon source fueled with D_2 and H_2 gas, electron density would reach a maximum at $B_0 \approx 200$ G then sharply fall off. This is not the case using Ar gas to fuel the discharge, which would show a linear increase in electron density past $B_0 = 1500$ G. That work then showed that the reduced ion mass moves the high-density limit of the lower hybrid resonance (HDLH), which reduces to the root of the product of the electron and ion cyclotron frequencies as $\omega_{HDLH} = \sqrt{\omega_{ce}\omega_{ci}}$, to lower magnetic field values. Operating in magnetic field values above the HDLH, $B_0 > 200$ G for D_2, restricts the slow-wave to the low electron density region of the plasma column and the helicon wave to the high-density region, thus creating a region in the plasma that is evanescent to both waves.

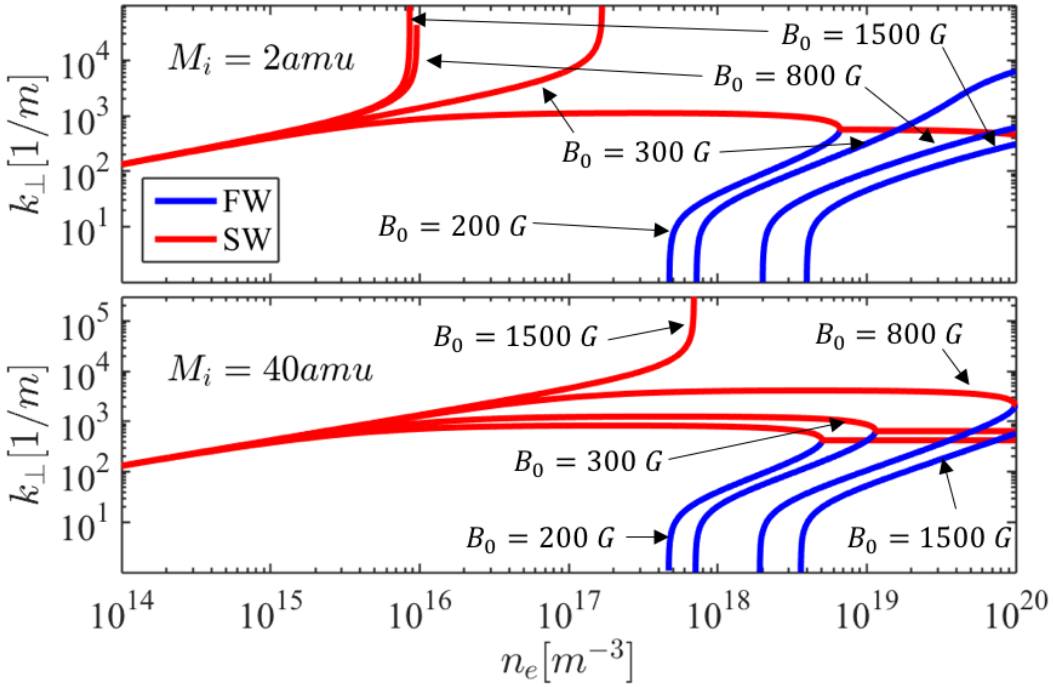

Figure 5.1: Perpendicular wavelength solved calculated from the positive (SW) and negative (FW) roots of Eq. 2.30 assuming $k_z = 20\ \frac{1}{m}$ for Deuterium (top) and Argon (bottom) ions. Plotted as a function of electron density for 4 values of magnetic field strength.

Fig. 5.1 shows the effect of lower ion mass on the solution of Eq. 2.30 for different values of magnetic field. For a plasma with D_2 ions an evanescent gap between the FW and SW branches is formed for $B_0 > 200$ G. For a plasma with Ar ions the evanescent gap does not form in the plasma column until $B_0 > 1500$ G.

5.1.2 Dispersion Relation Under the Helicon Antenna

Fig. 5.2 displays (top) the cold plasma dispersion relation, relevant to the experimental conditions in configuration B, as a function of electron density and (bottom) a typical radial electron density profile associated with Fig. 5.2 measured at the helicon source (location A in Fig. 3.4). Since the lower hybrid resonance (LHR) restricts the propagation of the slow-wave to the edge region where the electron density is less than $10^{16}\ m^{-3}$, any power deposition and/or RF wave fields in the plasma core are attributed to the fast-wave.

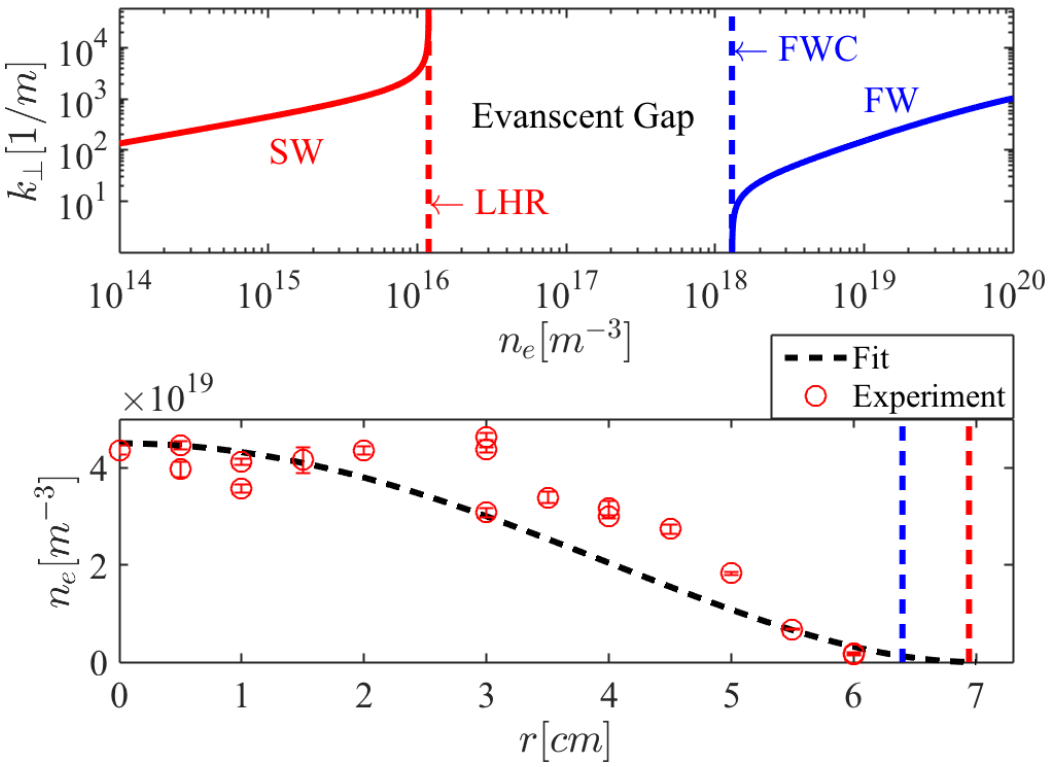

Figure 5.2: (Top) Perpendicular wavelength of the slow-wave (SW) and the fast-wave (FW) calculated from the cold plasma dispersion relation assuming $k_z = 20\ m^{-1}$, $B_0 = 0.05$ T, and atomic deuterium ions. (Bottom) Electron density radial profile measured at location A from Fig. 3.4. The radial locations of the lower hybrid resonance (LHR) and the fast-wave cutoff (FWC) are shown assuming an electron density profile fit of $n_e(r) = n_e^{max}\left(1-(r/R_p)^2\right)^2 + n_e^{edge}$ where $n_e^{max} = 4.5\times10^{19}\ m^{-3}$, $n_e^{edge} = 1\times10^{16}\ m^{-3}$, and $R_p = 7$ cm.

From Fig. 5.2 (bottom) we see that the SW in the discharge is restricted to the periphery of the plasma. Here the electron density is fit to fall to a value of $1\times10^{16}\ m^{-3}$. However the Langmuir probes in Proto-MPEX do not resolve the low electron density in the edge so the value is assumed

5.1.3 Dispersion Relation in 2D

Fig. 5.3 shows the regions of propagation for a FW and SW for typical parameters used in the simulation. The region of propagation of the SW is restricted to the outer edge of the plasma where the electron density is low enough. The FW is restricted to the high density region of the plasma column. The evanescent gap where neither FW or SW can propagate is also clear here.

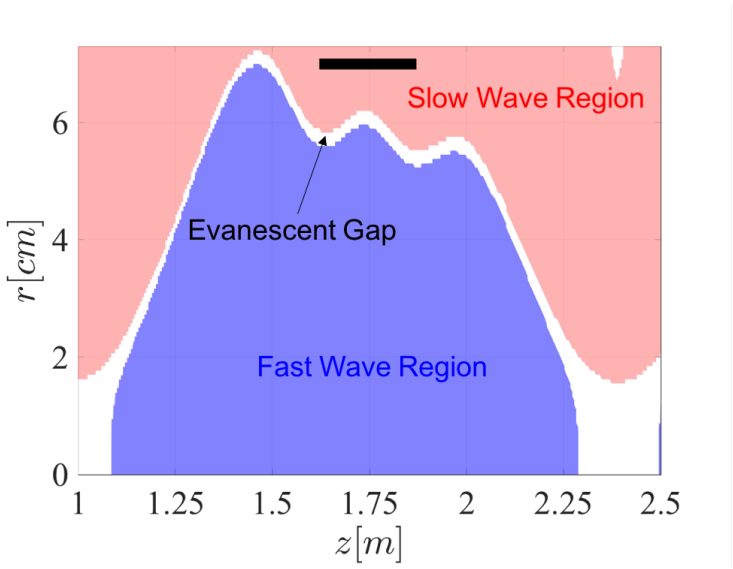

Figure 5.3: Contours of perpendicular wavelength ($k_\perp$) solved for from Eq. 2.30 assuming $k_z = 20\ m^{-1}$ and electron density defined by Eq. 4.14 using $n_{e_{peak}} = 2.7 \times 10^{19}\ m^3$. The magnetic field is solved for with the current coils set in configuration A with $I_H = 260$ A. The blue contour represents where $k_\perp$ for the fast-wave solution is non-zero. The red contour represents where $k_\perp$ for the slow-wave solution is non-zero. The evanescent region, $k_\perp = 0$ for both waves, is represented by the white contour. The location of the helicon antenna is represented by the thick black line.

Fig. 5.3 reveals an interesting consequence of the magnetic geometry. The FW is cutoff because of the high magnetic field strength present in the magnetic mirror. This results in a formation of a cavity for the FW in the region under the helicon antenna. Throughout the results section it is apparent that the FW does not propagate past the magnetic mirror in this magnetic configuration.

5.1.4 FW Normal Mode Dispersion Relation

In section 2.4 the bounded wave theory was described and dispersion relations for a cylindrically bound FW (helicon mode) and SW (TG mode) were derived. In the following sections special attention is paid to the SW anti-resonance condition when normal modes of the FW are satisfied. The dispersion relation for helicon normal modes can be written by setting Eq. 2.81 to 0. Writing the above stated condition explicitly:

$$J'_m(k_{\perp H}R_p) + \frac{m}{k_z R_p} J_m(k_{\perp H}R_p) = 0 \tag{5.1}$$

$$k_{\perp H} = \frac{\omega_{pe}^2 k_0^2}{\omega \omega_{ce} k_z} \tag{5.2}$$

Eq. 5.2 is just the rewritten form of Eq. 2.65 neglecting the collision frequency. Simplifying Eq. 5.1 using the long wavelength approximation ($k_z R_p \geq 1$) gives a convenient form that allows writing the electron density as a function of the magnetic field as:

$$n_e = \frac{c^2 \epsilon_0}{q} \left(\frac{B_0 k_z}{\omega R_p} \right) \left(p_{mi} - \frac{k_z R_p}{m} \right) \tag{5.3}$$

Eq. 5.3 is the dispersion relation for FW normal modes. This convenient form allows a discussion of the effects of changing the background magnetic field (B_0), the axial wavenumber (k_z), the azimuthal mode number (m), and the plasma radius (R_p). The i^{th} root of the Bessel function dictates which order radial mode satisfies this dispersion relation.

5.2 Core Power Deposition Contours

Understanding how the antenna couples power to the steady-state plasma is important for predicting the density limitations of the helicon source. Light ion helicon authors have attributed successful high electron density production to excitation of helicon normal modes in the plasma column[26, 23]. In section 2.4 it is described that in a more complicated geometry resonant behavior of the fast-wave does not exist. However, the bounded dispersion relation derived by this approach predicts anti-resonance regimes of the slow-wave. In anti-resonance, the non-resonant mode conversion of the fast-wave to the slow-wave is suppressed. This condition allows the fast-wave to couple more power into the core plasma. In Fig. 5.4 contours of normalized core power deposition are plotted as predicted by the simulation described above. The experimentally relevant parameter space is outlined by the red box. Inside the experimentally relevant parameter space points of maximum core power deposition are identified. These points form 3 distinct lines in $n_e(B_0)$. Since linear behavior in the peak core power deposition is predicted by the FW normal mode equation, Eq. (5.3, these solutions are referred to as normal mode solutions. The normal mode solutions have the following similar characteristics: A) Significant RF amplitude is present behind the antenna B) Reduction of edge power deposition that is not due to inductive coupling. Discussion and an interpretation of these

characteristics will be presented. Contours of RF field amplitudes and contours of core power deposition will be compared for a typical normal mode solution, $n_{e_{peak}} = 2.7 \times 10^{19}\ m^3$ and $I_H = 260$ A, to a simulation with parameters corresponding to a minimum in power deposition, $n_{e_{peak}} = 2.8 \times 10^{19}\ m^3$ and $I_H = 560$. The latter solution is referred to as a TG mode solution because the slow-wave power deposition is more prevalent in these solutions.

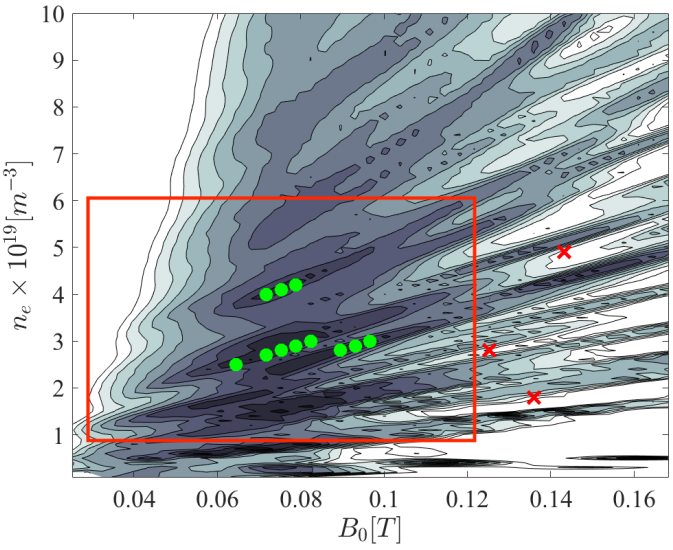

Figure 5.4: Contours of normalized core power deposition using a constant collision frequency of $\nu = \omega$. The area inside the red square marks the experimentally relevant parameters which will be the focus of the paper. The green circles mark peaks of core power deposition inside of the experimentally relevant parameter space. The red crosses mark areas of minimum core power deposition.

5.2.1 Effect of Collisions

Throughout this work, the normalized core power deposition is used as the figure of merit for identifying solutions that are normal modes of the plasma column. The core is defined as the region where $\chi < 0.5$. Fig. 5.5 shows how increasing the collision frequency (ν) reduces the sharpness of the power deposition peaks until they are destroyed. The collision frequency broadens the power deposition peaks because normal mode behavior in the discharge relies on the waves excited from the antenna to interfere constructively on-axis. If the collision frequency is high enough the wave excited by the antenna damps before it can interfere constructively on-axis. To identify the experimentally relevant normal modes the collision frequency will be held at a constant value of $\nu = \omega$, where ω is the driving frequency of the antenna, for the remainder of the analysis. At this value of ν the higher order k_z modes from the antenna spectrum are damped such that they do not contribute to the core power deposition but the main spectral features can still form normal

modes and structure in the core power deposition plots is still observed in Fig. 5.5.

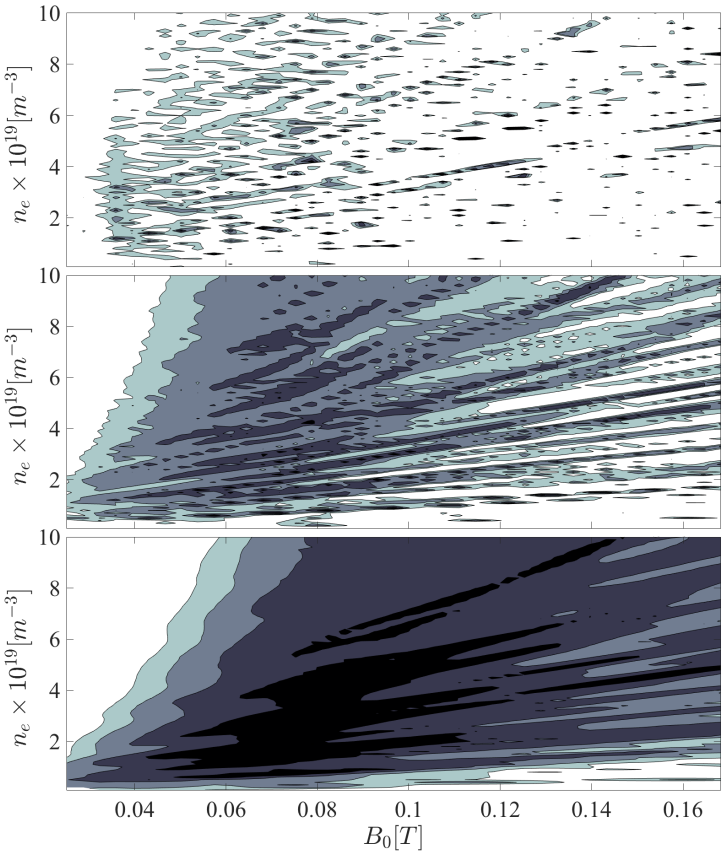

Figure 5.5: The effect of increasing collision frequency on the contours of core power deposition. Top $\nu = 0.05\omega$, middle $\nu = 0.25\omega$, bottom $\nu = \omega$. The contours show the log of the normalized power deposited in the core.

5.3 RF Field Analysis

In this section, the RF characteristic (k_z spectrum and $|B_z(r,z)|^2$ variation) of a normal mode solution will be compared to the RF characteristic of a TG-mode solution. Fig. 5.6 shows contours of $|B_z(r,z)|^2$ in real space and radial variation of $\bar{B}_z(r,k_z)$ for the normal mode solution and Fig. 5.7 show this data for the TG mode solution. Points along a constant line that are identified as normal modes have similar RF characteristic as other points along that line. Each constant line of normal mode solutions has an RF characteristic that is different from the other line of normal modes. This behavior is expected since the normal mode solutions must satisfy Eq. (5.3) which predicts linear behavior $n_e(B_0)$ if k_z, p_{mi}, R_p, and m are held constant.

The wave solution in real space a) of Fig. 5.6 shows that the fast wave is contained to the region between

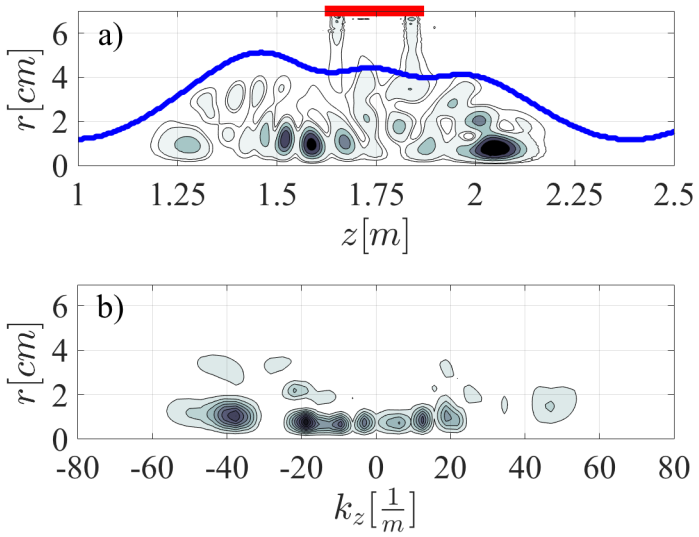

Figure 5.6: RF characteristic of the normal mode solution. a) Squared magnitude of the axial component of the RF magnetic field, $|B_z(r,z)|^2$. The blue contour line shows the location of $\chi = 0.5$. The red line shows the location of the helicon antenna. b) Discrete Fourier transform of the axial component of the RF magnetic field, $\bar{B}_z(r,k_z)$.

the magnetic mirrors, this is due to the fast wave cut off present at the large magnetic fields in the magnetic mirror. The presence of these magnetic mirrors creates a cavity for the fast wave, thus the fast-wave excited by the antenna can be reflected by the mirrors and interfere on-axis if it is not damped or loses energy to slow-wave mode conversion. Fig. 5.6 shows that the plasma spectrum contains waves with negative k_z indicating the fast wave excited has components traveling in $-\hat{z}$ as well as significant $|B_z|^2$ behind the antenna. Since the $m = +1$ mode of a helical turn antenna primarily excites waves with a positive k_z we can speculate that the waves excited for the normal mode simulation are reflected from the mirror and are allowed to interfere constructively on-axis.

The plasma spectrum of the TG mode solution, shown in Fig. 5.7, is dominated by waves with $k_z \approx +20\frac{1}{m}$ which is the dominant k_z feature of the $m = +1$ mode from the antenna vacuum spectrum. Also, there is no significant $|B_z|^2$ present behind the antenna. This is indicating that the fast-wave excited by the antenna is not effectively reflected by the magnetic mirror and does not constructively interfere on-axis. In the following section, we show evidence that this is due to the fast-wave mode converting to the slow-wave in the mirror region producing significant edge heating of the plasma.

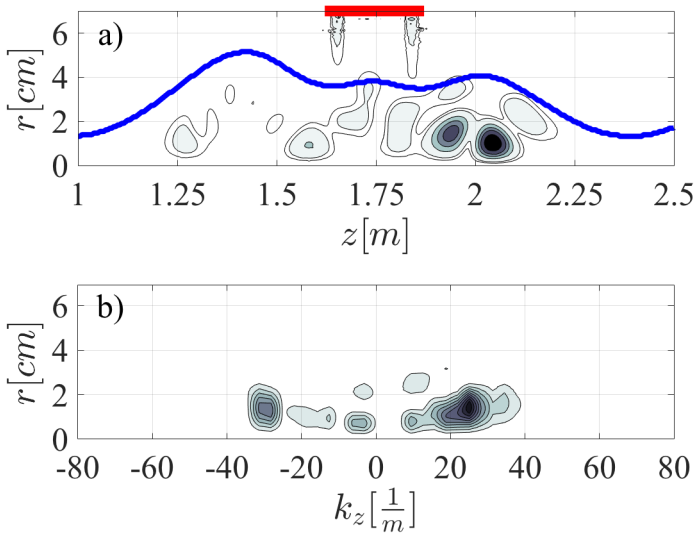

Figure 5.7: RF characteristic of the TG mode solution. a) Squared magnitude of the axial component of the RF magnetic field, $|B_z(r,z)|^2$. The blue contour line shows the location of $\chi = 0.5$. The red line shows the location of the helicon antenna. b) Discrete Fourier transform of the axial component of the RF magnetic field, $\bar{B}_z(r,k_z)$.

5.4 Power Deposition

Fig. 5.8 shows 2D contours of power loss density from the TG mode solution in Part a) and the normal mode solution in Part b). For $k_z = +20\frac{1}{m}$ the dispersion relation allows only the fast-wave to propagate in the core ($\chi < 0.5$) and the slow-wave is contained to the edge ($\chi 1.0$). Thus, the core power deposition is attributed solely to collisional damping of the fast-wave and edge power deposition is attributed to collisional damping of the slow-wave as well as inductive heating. The inductive heating is contained in the region directly under the antenna. Slow-wave heating that is excited by the antennas near fields is also present under the antenna. However, edge heating that is not located directly under the antenna is attributed to slow-wave excitation through non-resonant mode conversion of the fast-wave[22].

Fig. 5.4 shows that the normal mode solution contains significantly more power deposition in the core, while the TG mode solution contains more power deposition in the edge due to non-resonant mode conversion of the fast-wave. There is significant mode conversion that occurs in the mirror region, which is apparent by the power deposition present there for $\chi > 0.5$. This is consistent with the conclusion from the analysis of the RF characteristic of the TG solution. The fast-wave is not reflected effectively by the mirror since it losses its energy to the slow-wave in this region. This conclusion is also consistent with experimental observations that when there is a jump into the "helicon-mode" a shift from edge to core power dominated power deposition is observed[2, 23]. The integrated core power deposition for the normal mode solution is

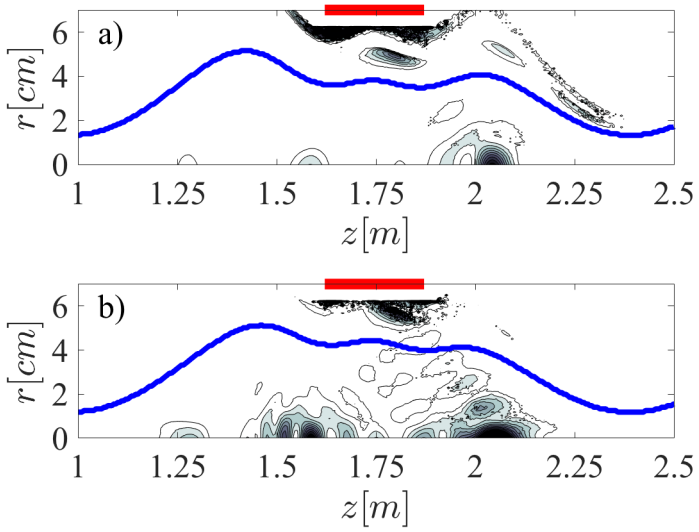

Figure 5.8: The 2D power loss density for the a) TG mode solution and b) normal mode solution. The blue contour line shows the location of $\chi = 0.5$. The red line shows the location of the helicon antenna.

43% of the total power deposited in the plasma, while for the TG solution that fraction of power deposition is reduced to 8%. Thus showing that operating the helicon antenna in a mode where it can effectively excite normal modes significantly increases the amount of core heating that the antenna provides.

Chapter 6

Conclusions and Future Work

This chapter will give an overview of the work presented in this thesis as well as propose extensions to this work. Section 6.1 will give an overview of the work presented here and make connections between experimental observations and simulation results. Extensions to this work are described in section 6.2. The extensions to this work include coupling this RF simulation with a plasma and neutral transport model such as the B2.5-Eirene model made for Proto-MPEX [42], a power balance method to predict equilibrium electron density for Proto-MPEX, and motivation for operating the helicon source at higher magnetic field strengths.

6.1 Conclusions

Throughout this thesis, we described the improved "helicon-mode" of operation in Proto-MPEX which is characterized by: (1) an increase in on-axis electron density up to $4 \times 10^{19}\ m^{-3}$ at the source location, (2) significant core power coupling, (3) suppression of edge power coupling and (4) an increase in the fast-wave energy density in the core plasma due to the (4) formation of a fast-wave radial eigenmode. The transition displays characteristics that are consistent with the plasma column entering a "slow-wave anti-resonance" regime as predicted by Shamrai and Taronov [17]. Experimental evidence to support this hypothesis are based on the IR thermography data as well as RF magnetic (B-dot) probe data. The IR thermography shows that the increase in core power deposition follows the suppression of the edge contribution. The B-dot probe data shows that concurrent with this power transition is an increase in on-axis magnetic energy and the formation of a radial normal mode patterns.

Next we have presented a 2D axisymmetric full wave model of the helicon antenna on Proto-MPEX. The 2D analytic antenna description represents the realistic antenna geometry as shown by comparison with a self-consistent vacuum simulation of the real geometry of the 3D antenna. The electron density profile used varies axially as a function of the magnetic flux which accurately describes the width of the plasma column.

Using this model, contours of maximum core power deposition were identified in the parameter space of

peak electron density and magnetic field strength. These contours take on a linear trend in this parameter space. The linear trend is understood as the plasma column satisfying the FW normal mode condition given by Eq. (5.3). The normal mode solutions responsible for these contours in the experimentally relevant parameter space are analyzed. The RF field and power deposition profiles of a normal mode solution are compared to a TG mode solution (point of minimum core power deposition). The normal mode solution seems to have significant negative k_z present in its plasma spectrum, as well as significant fast-wave amplitude in the region behind the antenna $z < 1.75$ m. Since the $m = +1$ azimuthal primarily drives positive k_z fast-waves we conclude that the magnetic mirror reflects the fast-wave propagating towards it which allows the constructive interference of the fast-wave in the plasma core. Therefore the magnetic mirrors act to form a cavity for the fast-wave. In the example of the TG solution, there is no evidence of significant wave reflection.

We then analyze the power deposition of the normal mode and TG solutuions and showed that the normal mode solution couples 43% of the total power into the core, whereas the TG solution only couples 8%. From the 2D power deposition contours of the TG solution, it is observed that there is significant edge heating present in the mirror region. This edge heating is not present in the mirror region for the case of the normal mode solution. These observations in the power deposition lead to the conclusion that for the case of the TG solution the fast-wave mode converts to the slow-wave in the mirror region, which leads to edge dominated power deposition in these solutions. Where as for the case of the helicon mode solution this mode conversion does not occur, this is also consistent with the picture of the anti-resonance regime predicted by Shamrai and Taronov [17]. However, in this more complicated 2D picture of a helicon antenna it seems as though the mirror region plays a critical role in the suppression of non-resonant mode conversion of the FW to the SW. This could be similar to the phenomena described by Virko et. al [43] where the inclination angle of the magnetic field was varied and when this angle exceeded the resonance group velocity angle the near antenna absorption fell and the power flux penetrated deep into the plasma. This mechanism could explain why light ion helicon plasmas have only been able to be operated successfully in the presence of a magnetic mirror [26, 27, 14, 2, 23].

6.2 Future Work

This model alone cannot predict the mechanisms responsible for the transition into the "helicon-mode". Coupling this RF model to a neutral gas and plasma transport simulation is required to shed light on the transition into the "helicon-mode". The neutral gas fueling dependence in achieving a "helicon-mode"

plasma is an open question that coupling these simulations would address. However, this RF model can be used to optimize the equilibrium state of the "helicon-mode" plasma in Proto-MPEX. Mainly, configuring the magnetic field inclination such that the fast-wave does not mode convert to the slow-wave at the periphery of the plasma so more power is available for density production in the core. In this chapter 3 extensions to this work will be described 1) coupling this simulation to a neutral gas and plasma transport model 2) a power balance method for predicting the equilibrium density, as proposed by Ref. Shamrai1998, and 3) the considerations and experimental changes for operating the helicon antenna at higher magnetic fields.

6.2.1 Mechanisms to the Transition to Helicon Mode

The physical mechanisms that drives the transition to the "helicon-mode" in Proto-MPEX is still an open question. Changing the neutral gas fueling from prefilling to gas puffing played a critical role in achieving the "helicon-mode" of operation. This suggests that there is a critical role the transport of neutrals play in the transition to the "helicon-mode".

Previous work has been done to couple neutral gas and plasma transport. Curreli and Chen [44, 21, 20] coupled neutral and plasma transport model to a full wave simulation to self consistently solve for the equilibrium density production inside of a helicon source. The assumption made on the electron density profile to follow the Boltzmann relation was made possible by assuming the short circuit effect to play the dominant role in cross-field transport of the electrons. This assumption on the electron transport is mediated by unmagnetized ions and a short discharge length; neither of these assumptions hold true for the case of Proto-MPEX. Also, Carter [38] coupled a full-wave solver to a single fluid treatment of the plasma density. In this work he concluded that the plasma pressure builds up near the periphery of the antenna where the power deposition takes place and plasma is transported radially inwards until the FW can propagate which then the power deposition becomes centrally peaked and the electron density increases. This simulation however made an assumption that $E_{\parallel} = 0$ which precludes excitation of the slow wave, therefor no mode-conversion could be observed in this treatment of the RF simulation. Also the neutral gas density was not modeled self consistently in Carter's treatment which avoids the issues of neutral gas depletion which is common in helicon sources [36, 37]. Therefore, to understand the complicated inter-play between the RF heating, the role of the neutral gas, as well as the roles of the electrons and ions that allow the equilibrium state of the "helicon-mode" in Proto-MPEX a 2D transport model that treats the neutral gas, ion, and electron fluids separately would be necessary. B2.5-Eirene code has been used to model the helicon source on Proto-MPEX [42]. However, the heating inputs in B2.5-Eirene are not self consistently coupled to an RF solver. An extension of the work in this thesis to understand the physical mechanisms that drive the

transition to the "helicon-mode" would be to couple an RF full-wave model such as the one described here to the B2.5-Eirene code.

6.2.2 Predicting Equilibrium Electron Density

The extension proposed in Section 6.2.1 is not a trivial one and requires a lot of resources and time to have a predictive model with the coupled physics of plasma, RF, and neutral transport. In this section a simplified model to predict equilibrium electron density produced by the helicon source on Proto-MPEX through a power balance of the electrons is proposed. This model was described by Shamrai in [22] and was used to predict abrupt density jumps observed in helicon sources. However, the model was not able to quantitatively reproduce electron density observations in helicon sources. The method is a power balance method, where the power absorbed by the plasma from the helicon source is balanced by the power losses associated with volumetric collisional losses, as well as convection and conduction losses.

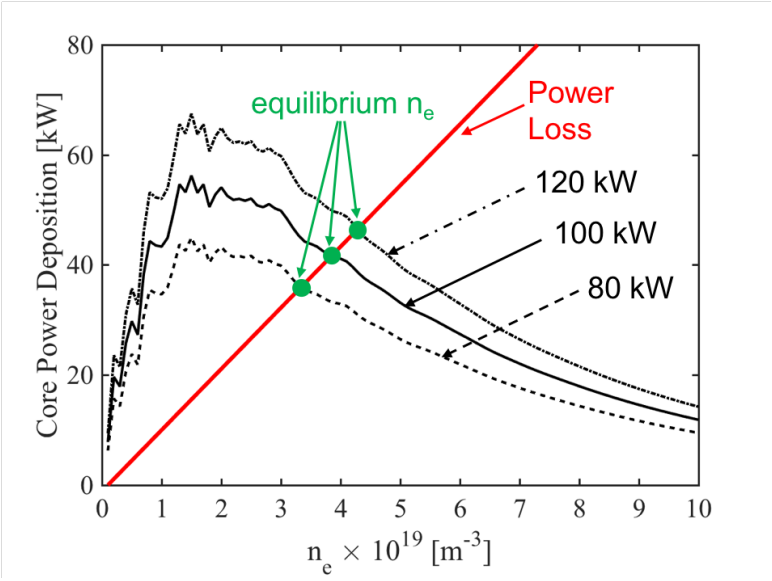

Figure 6.1: Core power absorption predicted by the full wave model for 3 different input powers. Power loss calculated as a function of electron density. Equilibrium electron density marked for different values of input power.

Fig. 6.1 shows the predicted power absorbed in the core plasma as a function of electron density for 3 different input power levels. The analytical power loss curve is in red. Where these curves intersect at an equilibrium location ($\frac{\partial P_{abs}}{\partial n} < \frac{\partial P_{loss}}{\partial n}$) the model predicts an equilibrium electron density value. The equilibrium electron density that this model would predict is marked by the green dots.

The power loss curve in Fig. 6.1 and Fig. 6.2 is arbitrary and not calculated correctly. Fig. 6.2 shows the predicted core power absorption for several values of magnetic field. The right figure shows the predicted

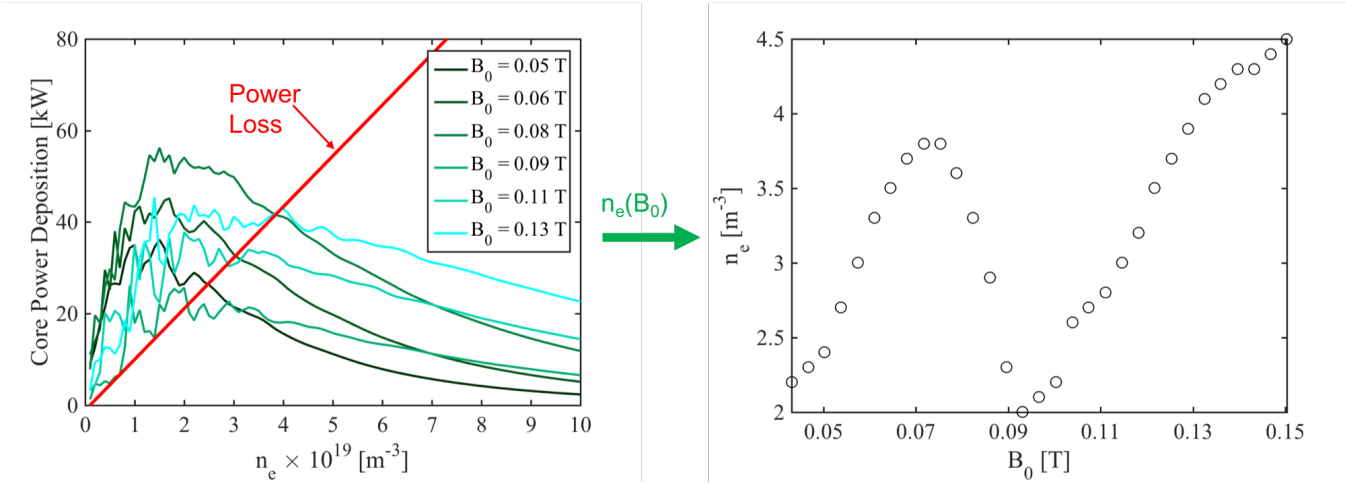

Figure 6.2: Left) Core power absorption predicted by the full wave model for several magnetic field values. Power loss calculated as a function of electron density. Right) Electron density predicted by the power balance method plotted as a function of magnetic field.

electron density as a function of magnetic field. We can see from Fig. 6.1 and Fig. 6.2 some of the scaling of equilibrium electron density with experimental parameters. The predicted equilibrium electron density from the simulation shows that the equilibrium electron density is expected to increase linearly with magnetic field strength as it does in the experiment until about 700 Gauss and then falls off steeply. This is consistent with the experiment, However it is predicting another increase in electron density at higher magnetic field, which is not observed experimentally. The power loss curve is arbitrary for now but a proper treatment of this with empirically calculated quantities is saved for future work. Setting up experiments to test if a second equilibrium density curve is available will be tested experimentally once the power capability is improved to 200 kW.

6.2.3 Operating at Higher Magnetic Field Strength

Operating the helicon source on Proto-MPEX at higher magnetic field would be beneficial because the electron density in Proto-MPEX has been shown to be a function of the magnetic flux. The width of the plasma is determined by the limiting flux line, which is typically under the helicon antenna and is determined by the magnetic field strength under the helicon antenna. So the ratio of the magnetic field under the helicon to the magnetic field strength downstream of the helicon antenna determines the width of the plasma column. Then to have a wider plasma in Proto-MPEX we need either a higher magnetic field under the helicon antenna or a lower magnetic field downstream of the helicon antenna. Since a lower magnetic field downstream of the helicon antenna is incompatible with the ion cyclotron heating, then we will need to increase the magnetic field under the helicon antenna if a wider plasma column is to be achieved.

Fig. 6.2 shows preliminary predictions of the scaling of equilibrium electron density with magnetic, which predicts another high density region for the Proto-MPEX helicon source at higher magnetic field. Fig. 3.10 shows that in experiment density production falls off after 700 Gauss and does not recover. Some theories for why this region is not observed experimentally is that not enough power is available to observe this second electron density production region. To test this an upgrade of the power availability will be increased from 100 kW to 200 kW.

This appendix will present som additional work concerning the tensor rotation as well as validation of the plasma tensor implemented in COMSOL. Section A will present the details of rotating the plasma tensor to the magnetic field reference. Validation of the plasma tensor implemented in the COMSOL simulation is presented in section B.

Appendix A

Tensor Rotation

This section will go over rotating the STIX tensor given by Eq. 4.17 from the Cartesian coordinate system to a local magnetic coordinate system. A schematic of the different coordinate systems is given by Fig. A.1. The final coordinate system is aligned in the reference frame of the magnetic field vector $\vec{B}_0$.

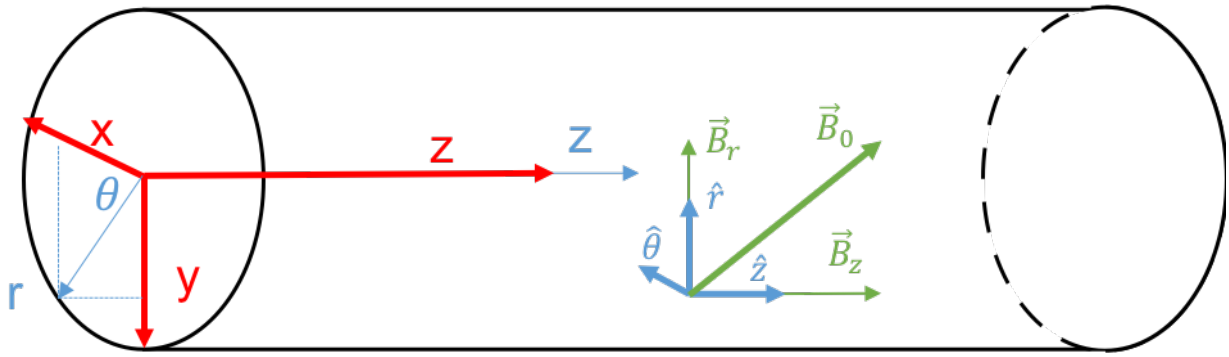

Figure A.1: Schematic of coordinate system transformation. Red coordinates show Cartesian coordinate system in which the STIX tensor is derived. Blue coordinates are the cylindrical coordinates (at $\theta = 0$ reduces to Cartesian coordinates). Green coordinates are the local magnetic coordinates.

First, Eq. 4.17 is rotated into a cylindrical coordinate system which given by Eq. A.1.

$$\overleftrightarrow{K}_{r\theta z} = \overleftrightarrow{Q}_z \overleftrightarrow{K} \overleftrightarrow{Q}_z^T \tag{A.1}$$

$$\overleftrightarrow{Q}_z = \begin{bmatrix} cos(\theta) & -sin(\theta) & 0 \\ sin(\theta) & cos(\theta) & 0 \\ 0 & 0 & 1 \end{bmatrix} \tag{A.2}$$

Where θ is the azimuthal angle, we can see from this that in the plane where $\theta = 0$ the STIX tensor is the same as Cartesian coordinate system since $\overleftrightarrow{Q}_z = \overleftrightarrow{I}$. Next we rotate the coordinate system to the local magnetic coordinates. Where we define the angle of the magnetic field from the $\hat{z}$ direction by $\phi = tan^{-1}\left(\frac{B_r}{B_z}\right)$. Similar to Eq. A.1 the rotation to the local magnetic coordinate system is then:

$$\overleftrightarrow{K}_{B_0} = \overleftrightarrow{Q}_{\phi}\overleftrightarrow{K}_{r\theta z}\overleftrightarrow{Q}_{\phi}^{T} \tag{A.3}$$

$$\overleftrightarrow{Q}_{\phi} = \begin{bmatrix} cos(\phi) & 0 & sin(\phi) \\ 0 & 1 & 0 \\ -sin(\phi) & 0 & cos(\phi) \end{bmatrix} \tag{A.4}$$

The tensor can be written as:

$$\overleftrightarrow{K}_{B_0} = \begin{bmatrix} \epsilon_{11} & \epsilon_{12} & \epsilon_{13} \\ \epsilon_{21} & \epsilon_{22} & \epsilon_{23} \\ \epsilon_{31} & \epsilon_{32} & \epsilon_{33} \end{bmatrix} \tag{A.5}$$

$$\epsilon_{11} = (\lambda)cos\phi^2 + (P)sin\phi^2 \tag{A.6}$$

$$\epsilon_{12} = -(\alpha)cos\phi \tag{A.7}$$

$$\epsilon_{31} = (P)cos\phi sin\phi - (\lambda)cos\phi sin\phi \tag{A.8}$$

$$\epsilon_{21} = (\alpha)cos\phi \tag{A.9}$$

$$\epsilon_{22} = (\lambda) \tag{A.10}$$

$$\epsilon_{23} = -(\alpha)sin\phi \tag{A.11}$$

$$\epsilon_{31} = (P)cos\phi sin\phi - (\lambda)cos\phi sin\phi \tag{A.12}$$

$$\epsilon_{32} = (\alpha)sin\phi \tag{A.13}$$

$$\epsilon_{33} = (\lambda)sin\phi^2 + (P)cos\phi^2 \tag{A.14}$$

$$\lambda = cos\theta(\chi) + sin\theta(\Lambda) \tag{A.15}$$

$$\alpha = cos\theta(\Lambda) - sin\theta(\chi) \tag{A.16}$$

$$\chi = (S)cos\theta - (iD)sin\theta \tag{A.17}$$

$$\Lambda = (iD)cos\theta + (S)sin\theta \tag{A.18}$$

Appendix B

Plasma Tensor Validation

A tensor has been derived to represent a cold plasma, now the tensor is implemented in COMSOL multi-physics and validate against dispersion calculations. A wave is excited in an infinite homogeneous plasma in COMSOL and the wavelength is compared to the predictions from the dispersion relation to validate the COMSOL implementation.

The rotated tensor was validated by rotating the the geometry and the source to be in the proper orientation with the magnetic field. Fig B.1 and B.2 show that the model agreed with the dispersion relation at all the rotation angles tested for both parallel and perpendicular propagation cases. In Fig. B.1 the perpendicular propagation case the ordinary wave encounters the $P = 0$ cutoff, while the extraordinary wave encounters $R = 0$ cutoff, $S = 0$ resonance, and $L = 0$ cutoff. We see that they interact with these layers as expected.

In Fig. B.2 the parallel propagation case was validated and the right-handed wave does not encounter any singularities in the index of refraction, while the left-handed wave encounters the ion cyclotron resonance.

The sources and wave polarization must also be rotated when rotating the geometry, this is achieved by applying the same rotation matrices to those vectors. Therefor the sources are rotated such that:

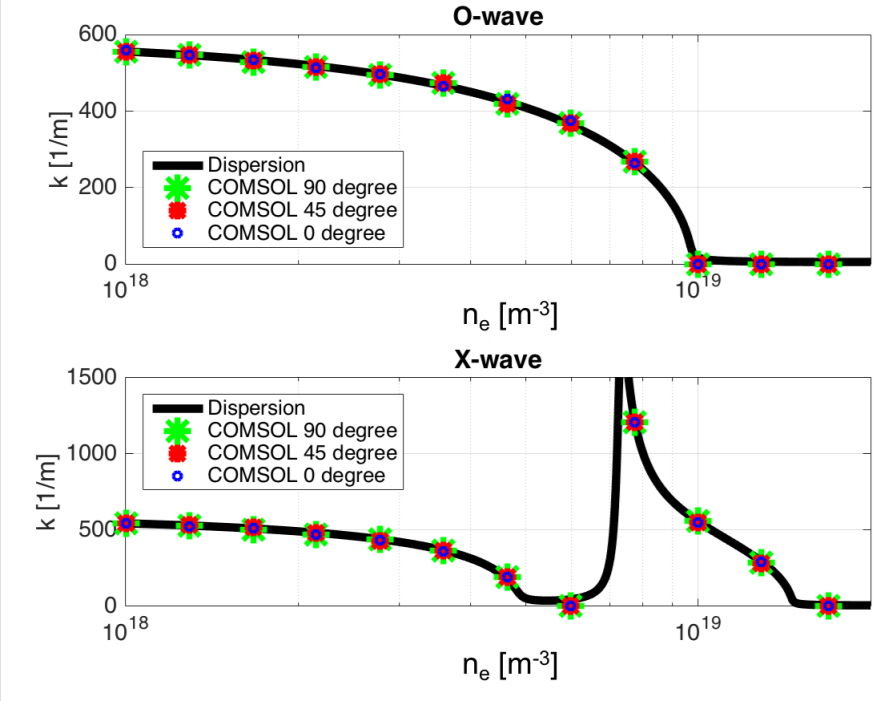

Figure B.1: Wave-number predicted from COMSOL simulations for perpendicular propagating waves. Ordinary wave dispersion versus COMSOL simulations (top). Extra-ordinary wave dispersion versus COMSOL simulation (bottom). Parameters used are $\omega = 2\pi(28\ GHz)$, $B_0 = 0.5$ T, $n_e = 1 \times 10^{18} to 2 \times 10^{19}\ m^{-3}$, and $m_i = m_D$. The tensor was tested at $\theta = 0°$ and $\phi = 0°, 45°$, and $90°$.

$$E_L = \overleftrightarrow{Q}_\phi \begin{bmatrix} 1 \\ -i \\ 0 \end{bmatrix} = \begin{bmatrix} cos\phi \\ -i \\ -sin\phi \end{bmatrix} \tag{B.1}$$

$$E_R = \overleftrightarrow{Q}_\phi \begin{bmatrix} 1 \\ i \\ 0 \end{bmatrix} = \begin{bmatrix} cos\phi \\ i \\ -sin\phi \end{bmatrix} \tag{B.2}$$

$$E_O = \overleftrightarrow{Q}_\phi \begin{bmatrix} 0 \\ 0 \\ 1 \end{bmatrix} = \begin{bmatrix} sin\phi \\ 0 \\ cos\phi \end{bmatrix} \tag{B.3}$$

$$E_X = \overleftrightarrow{Q}_\phi \begin{bmatrix} 0 \\ 1 \\ 0 \end{bmatrix} = \begin{bmatrix} 0 \\ 1 \\ 0 \end{bmatrix} \tag{B.4}$$

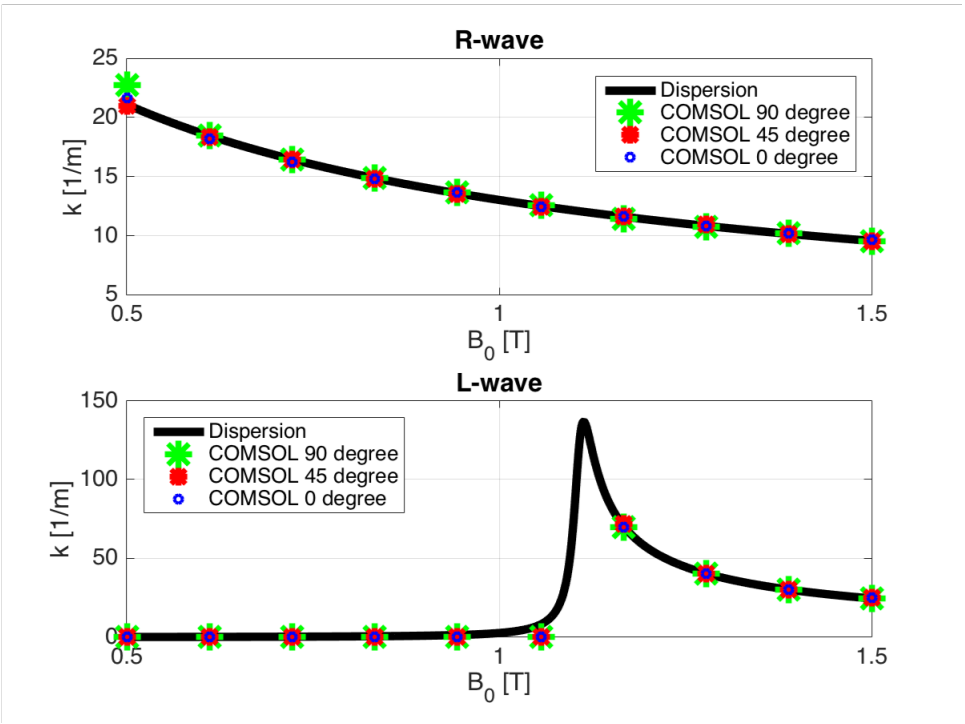

Figure B.2: Wave-number predicted from COMSOL simulations for parallel propagating waves. Right-handed wave dispersion versus COMSOL simulations (top). Left-handed wave dispersion versus COMSOL simulation (bottom). Parameters used are $\omega = 2\pi(8.5\ MHz)$, $B_0 = 0.5$ to 1.5 T, $n_e = 3 \times 10^{19}\ m^{-3}$, and $m_i = m_D$. The tensor was tested at $\theta = 0°$ and $\phi = 0°, 45°$, and $90°$.

References

[1] J. Rapp, T. M. Biewer, T. S. Bigelow, J. F. Caneses, J. B. Caughman, S. J. Diem, R. H. Goulding, R. C. Isler, A. Lumsdaine, C. J. Beers, T. Bjorholm, C. Bradley, J. M. Canik, D. Donovan, R. C. Duckworth, R. J. Ellis, V. Graves, D. Giuliano, D. L. Green, D. L. Hillis, R. H. Howard, N. Kafle, Y. Katoh, A. Lasa, T. Lessard, E. H. Martin, S. J. Meitner, G. N. Luo, W. D. McGinnis, L. W. Owen, H. B. Ray, G. C. Shaw, M. Showers, and V. Varma, "Developing the science and technology for the Material Plasma Exposure eXperiment," *Nuclear Fusion*, vol. 57, no. 11, 2017.

[2] J. B. O. Caughman, R. H. Goulding, T. M. Biewer, T. S. Bigelow, I. H. Campbell, J. Caneses, S. J. Diem, A. Fadnek, D. T. Fehling, R. C. Isler, E. H. Martin, C. M. Parish, J. Rapp, K. Wang, C. J. Beers, D. Donovan, N. Kafle, H. B. Ray, G. C. Shaw, and M. A. Showers, "Plasma Source Development for Fusion-Relevant Material Testing," *Journal of Vacuum Science & Technology A: Vacuum, Surfaces, and Films*, vol. 35, 2017.

[3] J. Rapp, T. Biewer, J. Canik, J. B. O. Caughman, R. H. Goulding, D. L. Hillis, J. Lore, and L. Owen, "No Title," *Fusion Science and Technology*, vol. 64, no. 2, pp. 237–244, 2013.

[4] R. Hazeltine, "Research needs for magnetic fusion energy sciences, Report of the Research needs Workshop (ReNeW)," tech. rep., DOE/OFES, Bethesda, Maryland, 2009.

[5] M. Greenwald, "Priorities, Gaps and Opportunities: Towards A Long-Range Strategic Plan For Magnetic Fusion Energy," tech. rep., Fusion Energy Sciences Advisory Committee, 2007.

[6] M. Greenwald, "Opportunities for Fusion Materials Science and Technology Research Now and During the ITER Era," tech. rep., DOE/Fusion Energy Sciences Advisory Committee, 2012.

[7] R. W. Boswell, "Plasma production using a standing helicon wave," *Physics Letters A*, vol. 33, no. 7, pp. 457–458, 1970.

[8] R. W. Boswell, "Very efficient plasma generation by whistler waves near the lower hybrid frequency," *Plasma Physics and Controlled Fusion*, vol. 26, no. 10, pp. 1147–1162, 1984.

[9] F. F. Chen and D. Arnush, "Generalized theory of helicon waves. I. Normal modes," *Physics of Plasmas*, vol. 4, no. 9, pp. 3411–3421, 1997.

[10] B. D. Hayden, D. R. Juliano, M. N. Neumann, J. P. Allain, and D. N. Ruzic, "No Title," *IEEE Transactions on Plasma Science*, vol. 25, no. 7, 1997.

[11] A. V. Arefiev and B. N. Breizman, "Theoretical components of the VASIMR plasma propulsion concept," *Physics of Plasmas*, vol. 11, no. 5 PART 2, pp. 2942–2949, 2004.

[12] J. P. Squire, "Investigation of a Light Gas Helicon Plasma Source for the VASIMR Space Propulsion System," *AIP Conference Proceedings*, vol. 694, pp. 423–426, 2003.

[13] J. Rapp, T. M. Biewer, T. Bigelow, J. B. O. Caughman, R. Duckworth, D. Giuliano, R. H. Goulding, D. L. Hillis, R. Howard, R. J. Ellis, T. Lessard, J. D. Lore, A. Lumsdaine, E. Martin, W. D. Mcginnis, S. J. Meitner, L. W. Owen, H. Ray, G. Shaw, and V. Varma, "The Material Plasma Exposure eXperiment MPEX : pre-design , development and testing of source concept," 2015.

[14] J. F. Caneses and B. D. Blackwell, "Collisional damping of helicon waves in a high density hydrogen linear plasma device," *Plasma Sources Science and Technology*, vol. 25, no. 5, p. 055027, 2016.

[15] J. Rapp, L. W. Owen, X. Bonnin, J. F. Caneses, J. M. Canik, C. Corr, and J. D. Lore, "Transport simulations of linear plasma generators with the B2.5-Eirene and EMC3-Eirene codes," *Journal of Nuclear Materials*, vol. 463, pp. 510–514, 2015.

[16] P. Fiflis, D. Andrucyzk, a. L. Roquemore, M. McGuire, D. Curreli, and D. N. Ruzic, "Lithium pellet production (LiPP): A device for the production of small spheres of lithium," *Review of Scientific Instruments*, vol. 84, no. 6, pp. 2013–2016, 2013.

[17] K. P. Shamrai and V. B. Taranov, "Volume and surface rf power absorption in a helicon plasma source," *Plasma Sources Sci. Technol.*, vol. 5, pp. 474–491, 1996.

[18] D. Arnush, "The role of TrivelpieceGould waves in antenna coupling to helicon waves," *Physics of Plasmas*, vol. 7, no. 7, p. 3042, 2000.

[19] D. D. Blackwell, T. G. Madziwa, D. Arnush, and F. F. Chen, "Evidence for Trivelpiece-Gould modes in a helicon discharge.," *Phys. Rev. Lett.*, vol. 88, no. 14, p. 145002, 2002.

[20] F. F. Chen and D. Curreli, "Central peaking of magnetized gas discharges," *Physics of Plasmas*, vol. 20, no. 5, 2013.

[21] D. Curreli and F. F. Chen, "Equilibrium theory of cylindrical discharges with special application to helicons," *Physics of Plasmas*, vol. 18, no. 11, 2011.

[22] K. P. Shamrai, "Stable modes and abrupt density jumps in a helicon plasma source," *Plasma Sources Sci. Technol.*, vol. 7, pp. 499–511, 1998.

[23] R. H. Goulding, J. B. O. Caughman, J. Rapp, T. M. Biewer, T. S. Bigelow, I. H. Campbell, J. F. Caneses, D. Donovan, N. Kafle, E. H. Martin, H. B. Ray, G. C. Shaw, and M. A. Showers, "Progress in the development of a high power helicon source for the Materials Plasma Exposure Experiment," *Fusion Science and Technology*, 2017.

[24] Y. Sakawa, T. Takino, and T. Shoji, "Contribution of slow waves on production of high-density plasmas by m=0 helicon waves," *Physics of Plasmas*, vol. 6, no. 12, p. 4759, 1999.

[25] M. Light, F. F. Chen, and P. L. Colestock, "Low frequency electrostatic instability in a helicon plasma," *Physics of Plasmas*, vol. 8, no. 10, pp. 4675–4689, 2001.

[26] Y. Mori, H. Nakashima, F. W. Baity, R. H. Goulding, M. D. Carter, and D. O. Sparks, "High density hydrogen helicon plasma in a non-uniform magnetic field," *Plasma Sources Science and Technology*, vol. 13, no. 3, pp. 424–435, 2004.

[27] M. Yoshitaka, N. Hideki, F. W. Baity, R. H. Goulding, M. D. Carter, and D. O. Sparks, "Focusing magnetic field contribution for helicon plasma on Mini-RFTF," *Thin Solid Films*, vol. 506-507, pp. 583–587, 2006.

[28] D. G. Swanson, "Plasma waves," *Plasma waves.*, no. January, p. 434, 1989.

[29] M. A. Lieberman and A. J. Lichtenberg, *Principles of Plasma Discharges and Materials Processing.* 2005.

[30] LXCAT, "Biagi database," 2017.

[31] F. F. Chen and D. D. Blackwell, "Upper Limit to Landau Damping in Helicon Discharges," *Physical Review Letters*, vol. 82, no. 13, pp. 2677–2680, 1999.

[32] T. H. Stix, *Waves in Plasmas.* AIP-Press, 1992.

[33] M. Light, I. D. Sudit, F. F. Chen, and D. Arnush, "Axial propagation of helicon waves," *Phys. Plasmas*, vol. 2, no. 11, p. 4094, 1995.

[34] M. Showers, T. M. Biewer, J. B. O. Caughman, D. C. Donovan, R. H. Goulding, and J. Rapp, "Heat flux estimates of power balance on Proto-MPEX with IR imaging," *Review of Scientific Instruments*, vol. 87, no. 11, p. 11D412, 2016.

[35] S. I. Braginskii, *Transport processes in a plasma*, vol. 1. 1965.

[36] A. W. Degeling, T. E. Sheridan, and R. W. Boswell, "Intense on-axis plasma production and associated relaxation oscillations in a large volume helicon source," *Physics of Plasmas*, vol. 6, no. 9, p. 3664, 1999.

[37] a. W. Degeling, T. E. Sheridan, and R. W. Boswell, "Model for relaxation oscillations in a helicon discharge," *Physics of Plasmas*, vol. 6, no. 5, p. 1641, 1999.

[38] M. D. Carter, F. W. Baity, G. C. Barber, R. H. Goulding, Y. Mori, D. O. Sparks, K. F. White, E. F. Jaeger, F. R. Chang-Díaz, and J. P. Squire, "Comparing experiments with modeling for light ion helicon plasma sources," *Physics of Plasmas*, vol. 9, no. 12, pp. 5097–5110, 2002.

[39] D. Arnush and F. F. Chen, "Generalized theory of helicon waves. II. Excitation and absorption," *Physics of Plasmas*, vol. 5, no. 5, p. 1239, 1998.

[40] S. Cho, "Eigenmode dispersion relations in radially inhomogeneous helicon plasmas," *Physics of Plasmas*, vol. 16, no. 6, 2009.

[41] Y. Mouzouris and J. E. Scharer, "ffects for Inductive asma Sources," vol. 24, no. 1, 1996.

[42] L. W. Owen, J. Rapp, J. Canik, and J. D. Lore, "Transport modeling of convection dominated helicon discharges in Proto-MPEX with the B2.5-Eirene code," *Physics of Plasmas*, vol. 24, no. 11, 2017.

[43] V. F. Virko, K. P. Shamrai, Y. V. Virko, and G. S. Kirichenko, "Wave phenomena, hot electrons, and enhanced plasma production in a helicon discharge in a converging magnetic field," *Physics of Plasmas*, vol. 11, no. 8, pp. 3888–3897, 2004.

[44] D. Curreli, "Transition from edge-localized to center-localized power deposition in helicon discharges," *EPJ Applied Physics*, vol. 56, no. 2, pp. 1–5, 2011.